Supplementary Information (SI) for Journal of Materials Chemistry A.

Electronic Supplementary Information for

In situ X-ray diffraction guided synthesis of Ni_2P nanoparticles for the Oxygen Evolution Reaction

Anders Bæk Borup,[a] Nhu-Quynh Thi Phan,[a] Magnus Kløve,[a] Andreas Dueholm Bertelsen,[a] Lise Joost Støckler,[a] and Bo Brummerstedt Iversen[a*]

[a]Center for Integrated Materials Research, Department of Chemistry and iNANO, Aarhus University, Langelandsgade 140, Aarhus 8000, Denmark

[*]Corresponding author: bo@chem.au.dk

Table of content

S1: In situ data

This section gives an overview of where the *in situ* data are collected and what wavelength is used. Due to the tendency for nickel phosphide to move in and out of the beam, resulting in sudden jumps in the intensity of the peaks, several experiments needed to be remeasured. Therefore, the *in situ* data are measured both at DanMAX, MAX IV, Lund, Sweden and P21.1, PETRA III, DESY, Hamburg, Germany according to Table 1. Table 1 also summarizes the wavelength used in each case.

Figure S1-S6 shows the collected PXRD data, and the fits of single frames used to identify the presence of Ni_2P and $Ni_{12}P_5$ respectively. During sequential Rietveld refinement, scale, unit cell dimensions (a, b, and c), and particle size are refined, while the atomic displacement parameters (APDs) are kept at 1 Å^2. Furthermore, it was necessary to refine strain for Ni_2P at 175 °C, 200 °C, 225 °C and 250 °C to obtain a good description. At 150 °C, the peaks were too weak to obtain a reliable refinement if both strain and size were refined, while the particles are no longer nanosized at 300 °C, making it unnecessary to refine strain.

Table S1. Overview of which beamline is used to collect the in situ diffraction data and the wavelength used.

Temperature (°C)	Beamline	Wavelength (Å)
150	P21.1, PETRA III, DESY, Hamburg, Germany	0.12222
175	DanMAX, MAX IV, Lund, Sweden	0.35424
200	DanMAX, MAX IV, Lund, Sweden	0.35424
225	DanMAX, MAX IV, Lund, Sweden	0.35424
250	P21.1, PETRA III, DESY, Hamburg, Germany	0.12222
300	DanMAX, MAX IV, Lund, Sweden	0.35424

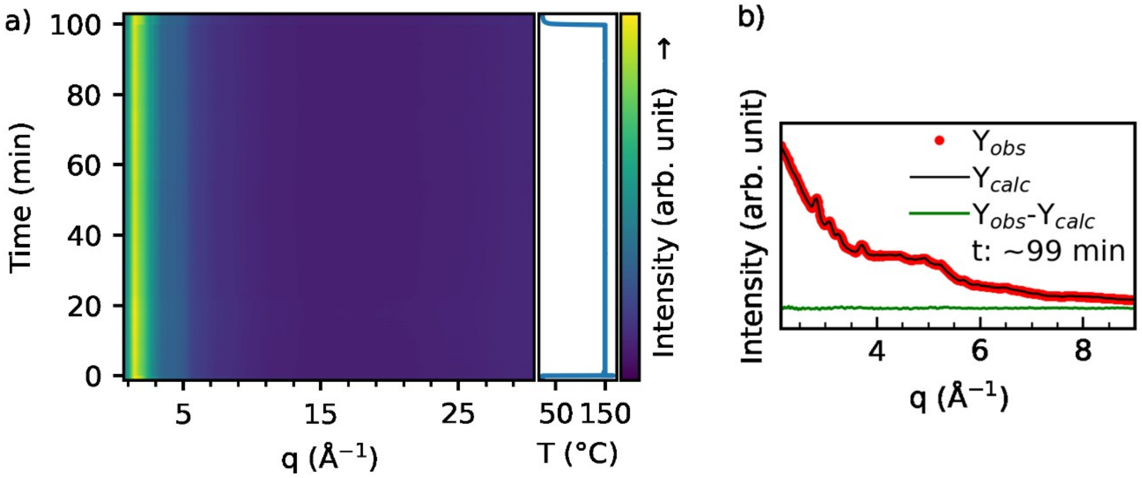

Figure S1. a) In situ diffraction data from the experiment at 150 °C, and b) the refined model of a single frame at t ≈ 99 min. Ni_2P is used to describe the diffraction data.

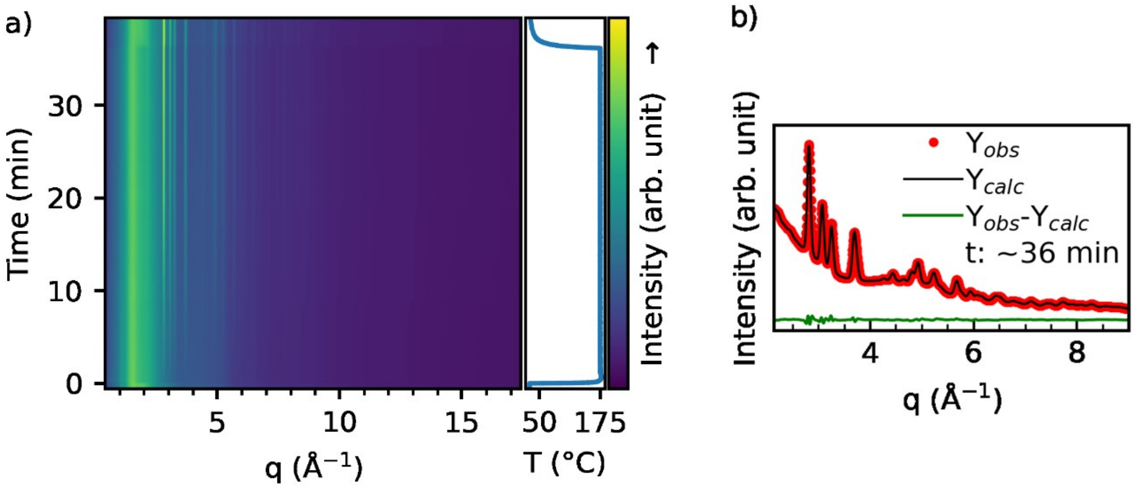

Figure S2. a) In situ diffraction data from the experiment at 175 °C, and b) the refined model of a single frame at t ≈ 36 min. Ni_2P is used to describe the diffraction data.

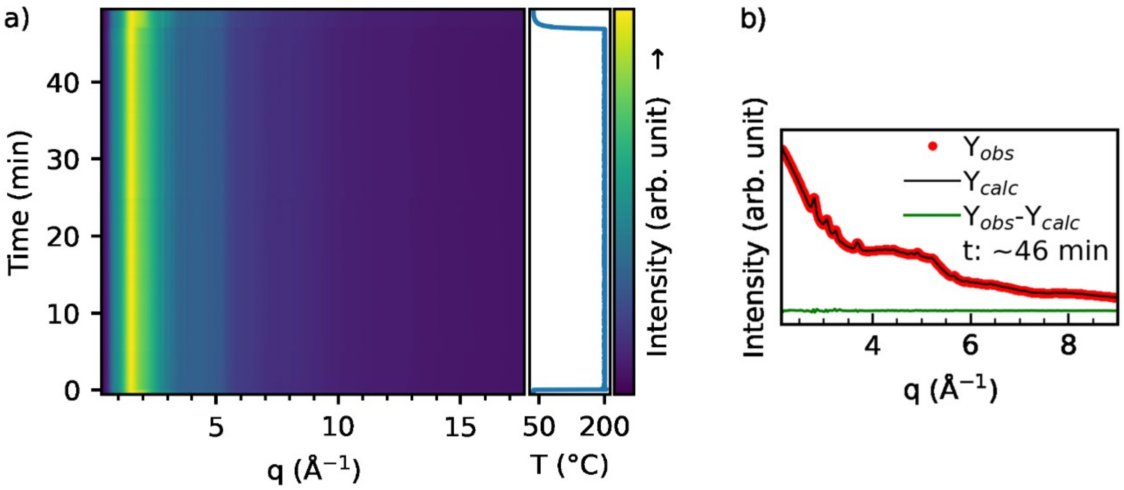

Figure S3. a) In situ diffraction data from the experiment at 200 °C, and b) the refined model of a single frame at t ≈ 46 min. Ni_2P is used to describe the diffraction data.

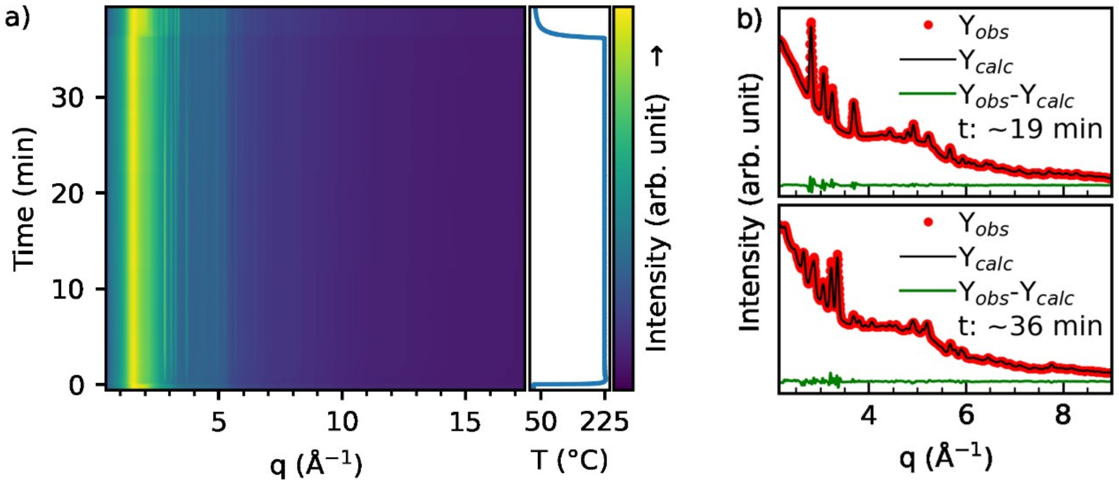

Figure S4. a) In situ diffraction data from the experiment at 225 °C, and b) the refined model of single frames at t ≈ 19 min and 36 min. At ~19 min Ni_2P is fitted, while $Ni_{12}P_5$ is fitted at ~36 min.

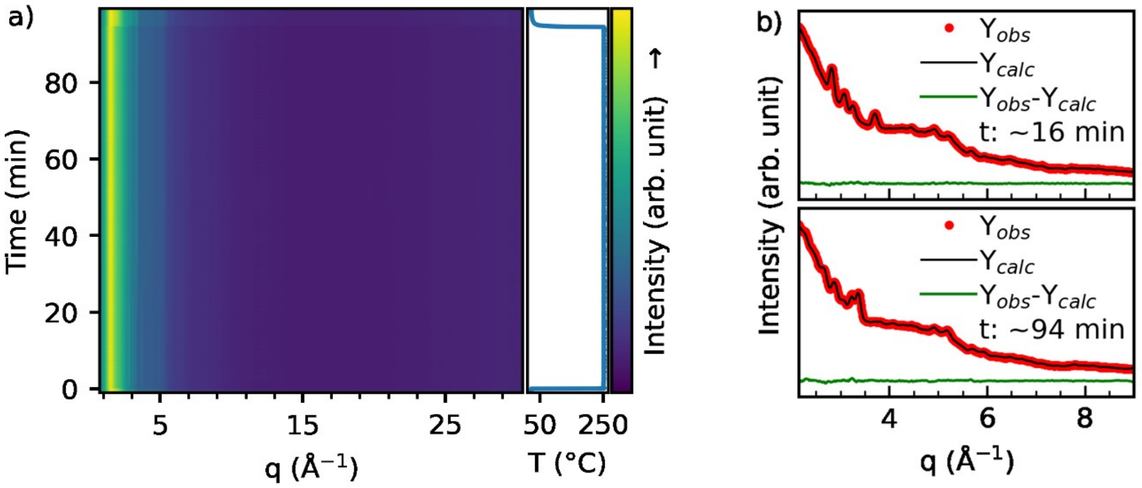

Figure S5. a) In situ diffraction data from the experiment at 250 °C, and b) the refined model of single frames at t ≈ 16 min and 94 min. At ~16 min Ni_2P is fitted, while $Ni_{12}P_5$ is fitted at ~94 min.

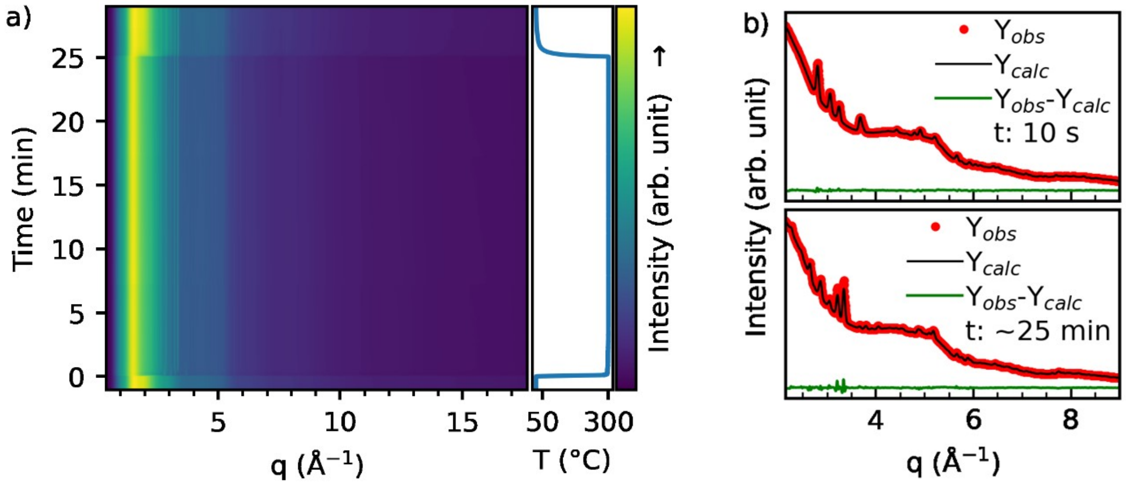

Figure S6. a) In situ diffraction data from the experiment at 300 °C, and b) the refined model of single frames at t = 10 s and ~25 min. At 10 s Ni_2P is fitted, while $Ni_{12}P_5$ is fitted at ~25 min.

S2: In situ results

The *in situ* results are shown in this section. Figure S7 shows the development in the scale factor during the *in situ* experiments for Ni_2P and $Ni_{12}P_5$. Figure S8 shows the evolution in particle size during the experiments. At 300 °C, the particles are no longer nano-sized, whereby they are omitted from Figure S8. Figures S9 and S10 show the unit cell dimensions during the *in situ* experiments for Ni_2P and $Ni_{12}P_5$, respectively, and compare them with literature-reported values. The literature-reported values are from room-temperature experiments,[1, 2] whereby the larger unit cells, observed during the *in situ* experiments, are due to thermal expansion.

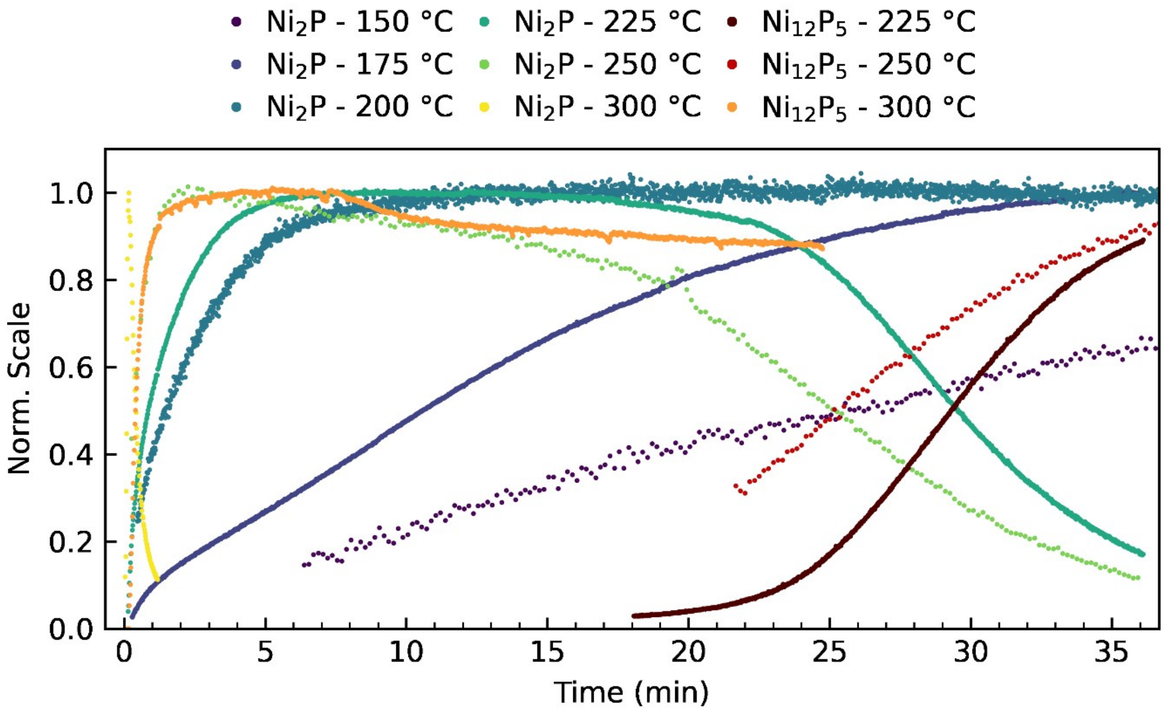

Figure S7. Development in scale factor for Ni_2P and $Ni_{12}P_5$ during the in situ experiments. The Ni_2P scale factors are ZMV weighted and normalized to 1 with the same normalization factor used to normalize the $Ni_{12}P_5$ ZMV weighted scale factors. For 150 °C and 250 °C, 10 data points are av*eraged.*

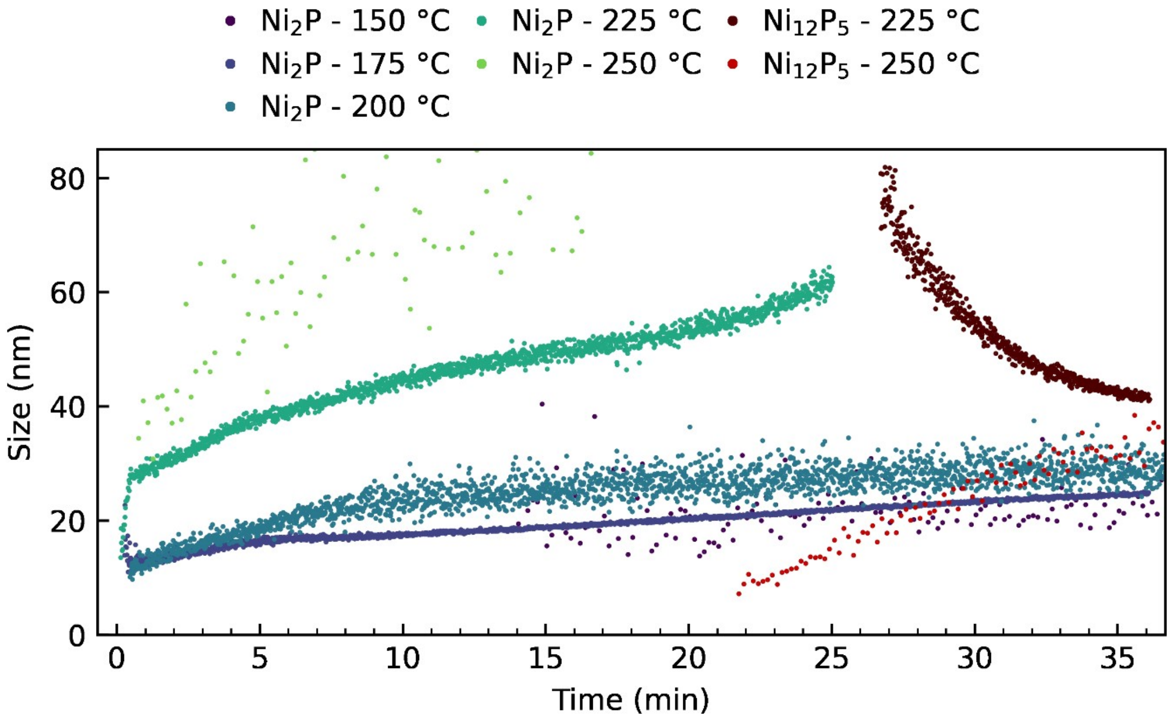

Figure S8. Particle size evolution during the in situ experiments. At 300 °C, the particles are no longer nano-sized, whereby they are omitted. For 150 °C and 250 °C, 10 data points are averaged.

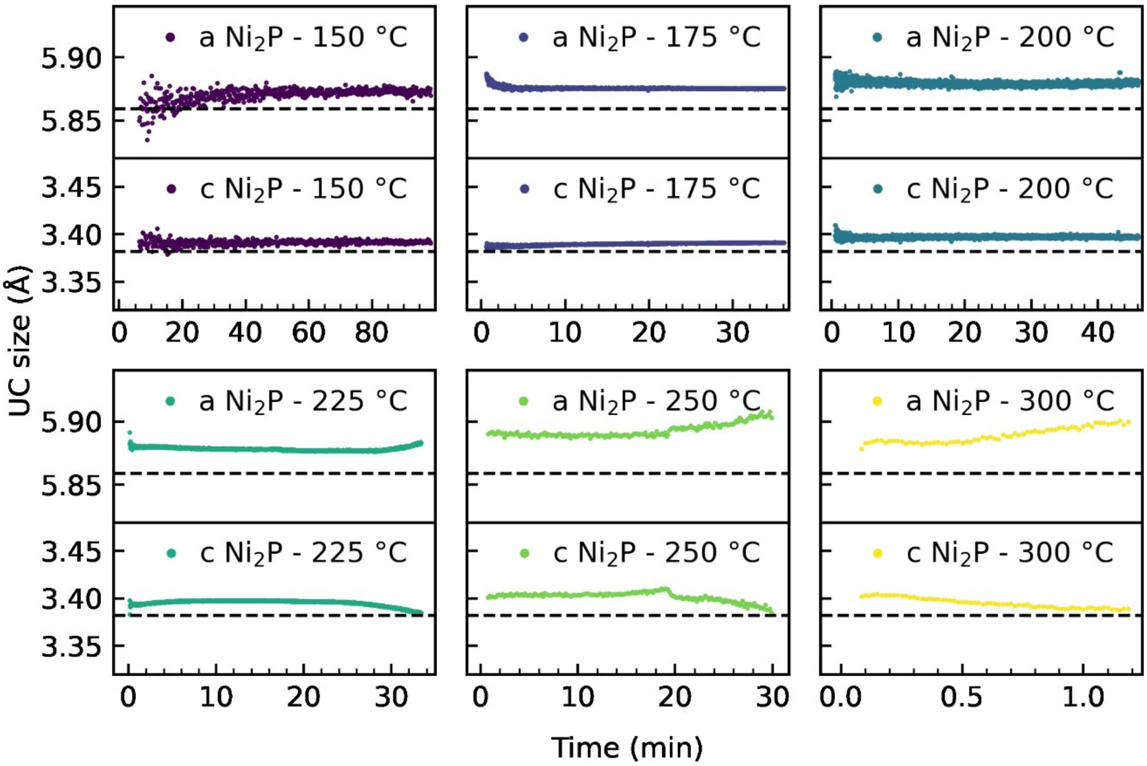

Figure S9. Development in unit cell dimensions for the hexagonal Ni$_2$P phase during the in situ experiments. For 150 °C and 250 °C, 10 data points are averaged. The unit cell dimensions are compared to literature-reported values from room-temperature experiments shown with dotted lines.

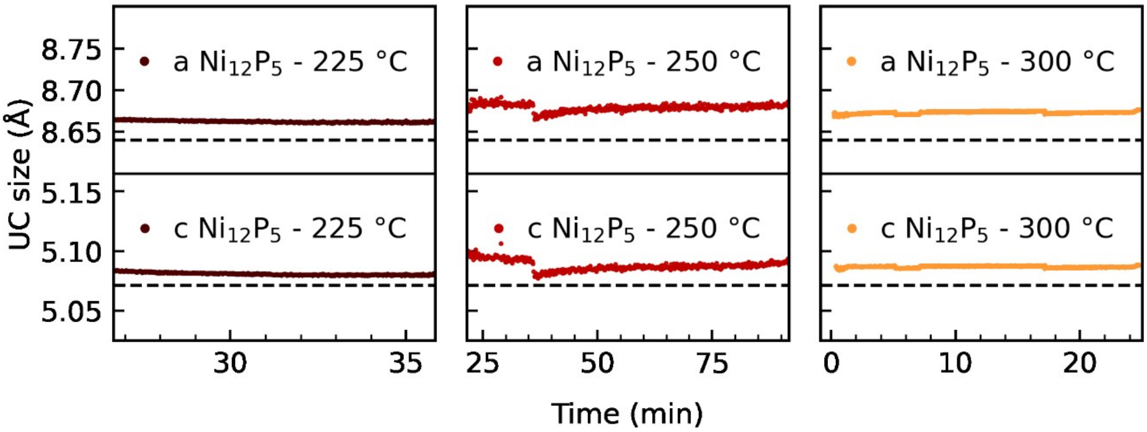

Figure S10. Development in unit cell dimensions for the tetragonal $Ni_{12}P_5$ phase during the in situ experiments. For 250 °C, 10 data points are averaged. The unit cell dimensions are compared to literature-reported values from room-temperature experiments shown with dotted lines. The small jump in unit cell size at the 250 °C experiment is due to the removal of the Ni_2P phase from the Rietveld Refinement.

S3: Results from kinetic analysis

This section lists the results from the kinetic analysis. The nucleation and growth (N&G) of Ni_2P have been modeled by a model containing both a nucleation term and a growth term (equation 1), while the phase transition from Ni_2P to $Ni_{12}P_5$ has been modeled with a growth term (equation 2). Table S2 summarizes the time intervals used to fit the models, while Tables S3 and S4 list the results for the N&G of Ni_2P and Ni_2P to $Ni_{12}P_5$ phase transition, respectively. Figure S11 shows the fits of the kinetic model to the Ni_2P to $Ni_{12}P_5$ phase transition.

Table S2. Time intervals used for the kinetic analysis.

T (°C)	$t_{N\&G\ Ni2P}$ (s)	$t_{Ni2P \rightarrow Ni12P5}$ (s)
150	377-5917	-
175	16 - 2165	-
200	28 - 2767	-
225	8 - 403	1083 - 2167
250	4 - 200	1300 - 5639
300	2 - 11	7 - 402

Table S3. Results from fitting the model to the N&G of Ni_2P. * The 300 °C results are removed from the determination of the activation energy due to the formation of $Ni_{12}P_5$ starting before the nucleation of Ni_2P stops, resulting in unrealistic values.

	150 °C	175 °C	200 °C	225 °C	250 °C	300 °C*
a (s)	1125(17)	604(3)	34(14)	30.3(5)	14.5(7)	-179
b (s)	1010(5)	393.1(9)	109(9)	72.7(3)	19.7(5)	6.7
k_g (s^{-1})	0.0180(15)	0.0116(3)	0.16(12)	0.0741(8)	0.28(3)	0.275(14)
n	0.44(3)	0.640(12)	0.35(7)	0.792(6)	0.96(11)	1.8(2)

Table S4. Results from modeling the Ni_2P to $Ni_{12}P_5$ phase transition.

	225 °C	250 °C	300 °C
k_g (s^{-1})	0.001039(11)	0.00127(13)	0.0402(8)
n	3.29(4)	1.8(2)	1.13(2)

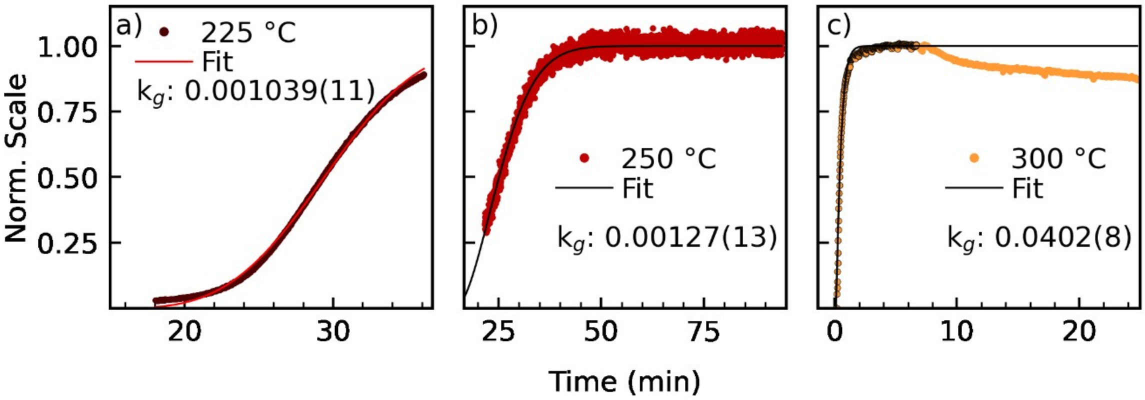

Figure S11. Fits of the kinetic model (equation 2) to the $Ni_{12}P_5$ normalized scale factor to describe the Ni_2P to $Ni_{12}P_5$ phase transition. In c), the dots with a black edge indicate the points used for the fit.

S4: Ex situ synthesis: overview and results

Table S5 gives an overview of *ex situ* experiments. It also states the phases present and corresponding particle size determined by powder X-ray diffraction. Figures S12 - S20 visually compare the fit from Rietveld refinement with the measured diffraction data.

Table S5. Results from Rietveld refinement of synthesis products from the ex situ experiments.

T (°C)	t (h)	Phase	a (Å)	c (Å)	Size (nm)	R_{wp}
150	2	100% Ni_2P	5.8752(9)	3.3886(7)	14.3(4)	1.85
150	4	100% Ni_2P	5.8704(5)	3.3873(4)	19.9(4)	3.66
150	24	100% Ni_2P	5.8696(1)	3.3902(1)	19.50(8)	3.55
200	2	100% Ni_2P	5.8702(7)	3.3874(5)	24.6(8)	2.80
200	4	100% Ni_2P	5.86725(8)	3.39006(6)	25.78(9)	3.71
200	24	100% Ni_2P	5.86652(6)	3.38980(4)	29.52(8)	3.69
240	2	100% Ni_2P	5.86675(7)	3.38985(5)	27.29(9)	3.82
240	4	82.10(6)% Ni_2P	5.86644(6)	3.39002(5)	30.9(1)	4.13
		17.90(6)% $Ni_{12}P_5$	8.6492(1)	5.07365(8)	70(1)	
240	24	34.46(1)% Ni_2P	5.8662(1)	3.3904(1)	36.0(5)	8.03
		65.54(1)% $Ni_{12}P_5$	8.64828(9)	5.07421(6)	108(1)	

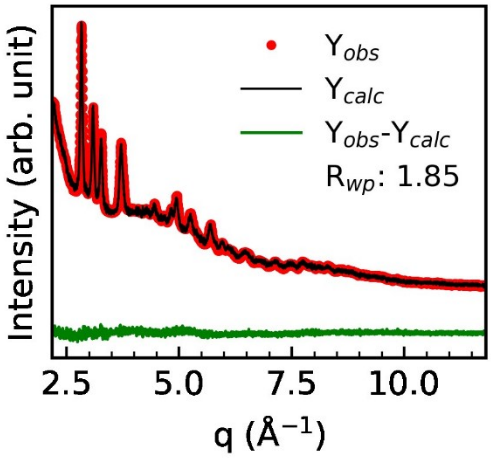

Figure S12. PXRD, 150 °C and 2 h.

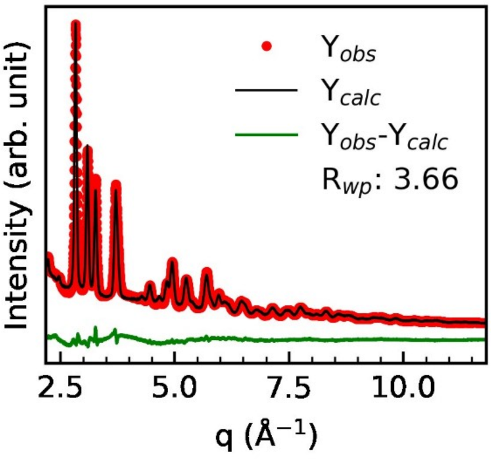

Figure S13. PXRD, 150 °C and 4 h.

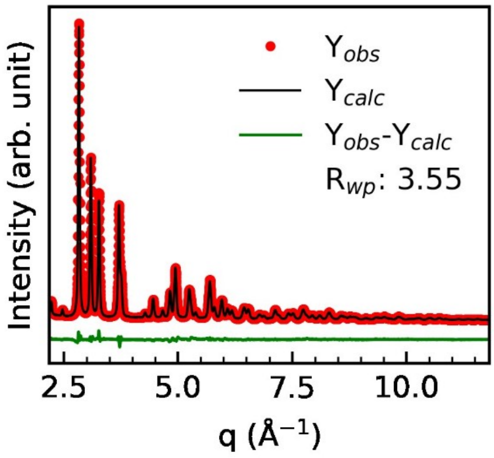

Figure S14. PXRD, 150 °C and 24 h.

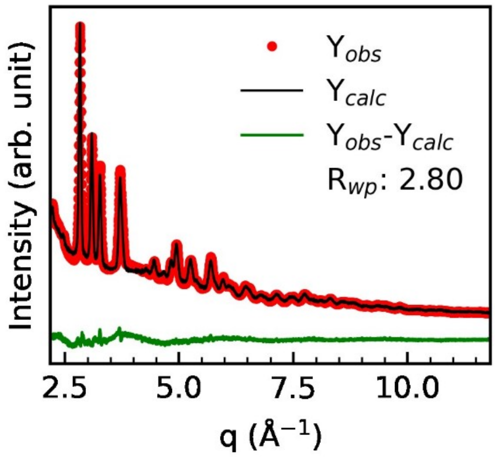

Figure S15. PXRD, 200 °C and 2 h.

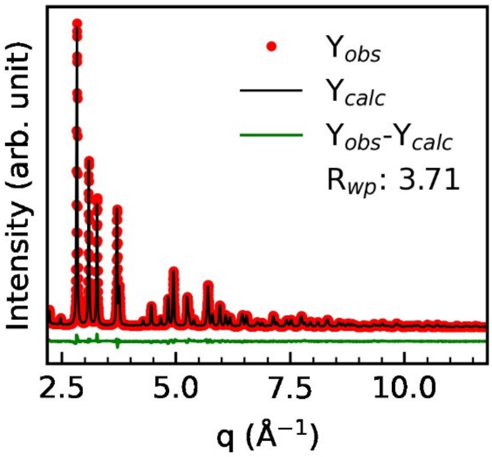

Figure S16. PXRD, 200 °C and 4 h.

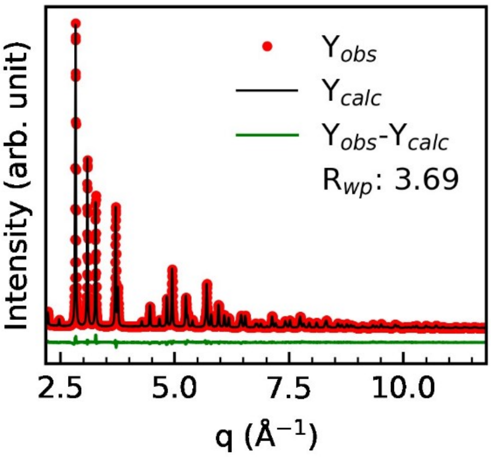

Figure S17. PXRD, 200 °C and 24 h.

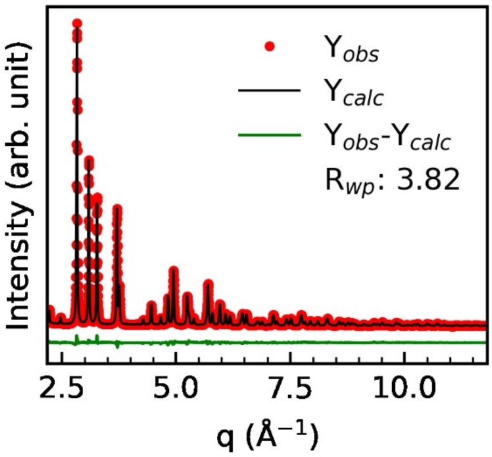

Figure S18. PXRD, 240 °C and 2 h.

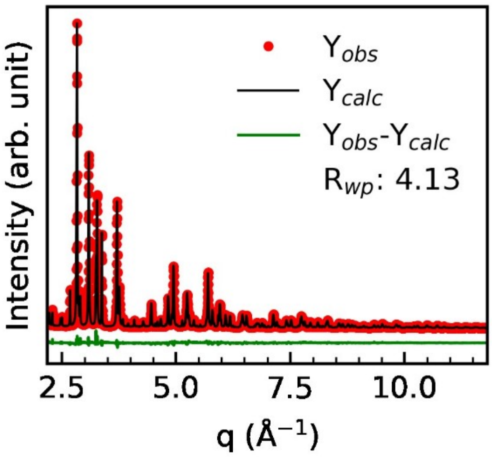

Figure S19. PXRD, 240°C and 4 h.

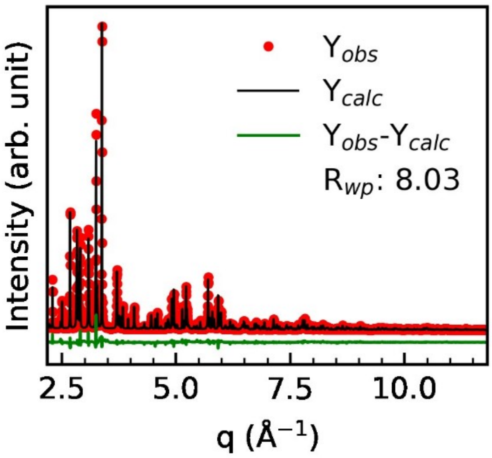

Figure S20. PXRD, 240 °C and 24 h.

S5: Determination of crystallinity

The crystallinity is determined as described in the main article. This section quickly illustrates the fits from where the crystallinity is determined. Figure S21 shows the fits as well as the contribution from Al_2O_3 and Ni_2P to the diffractogram. It furthermore summarizes the weight percent of each phase as well as the crystallinity of the different samples.

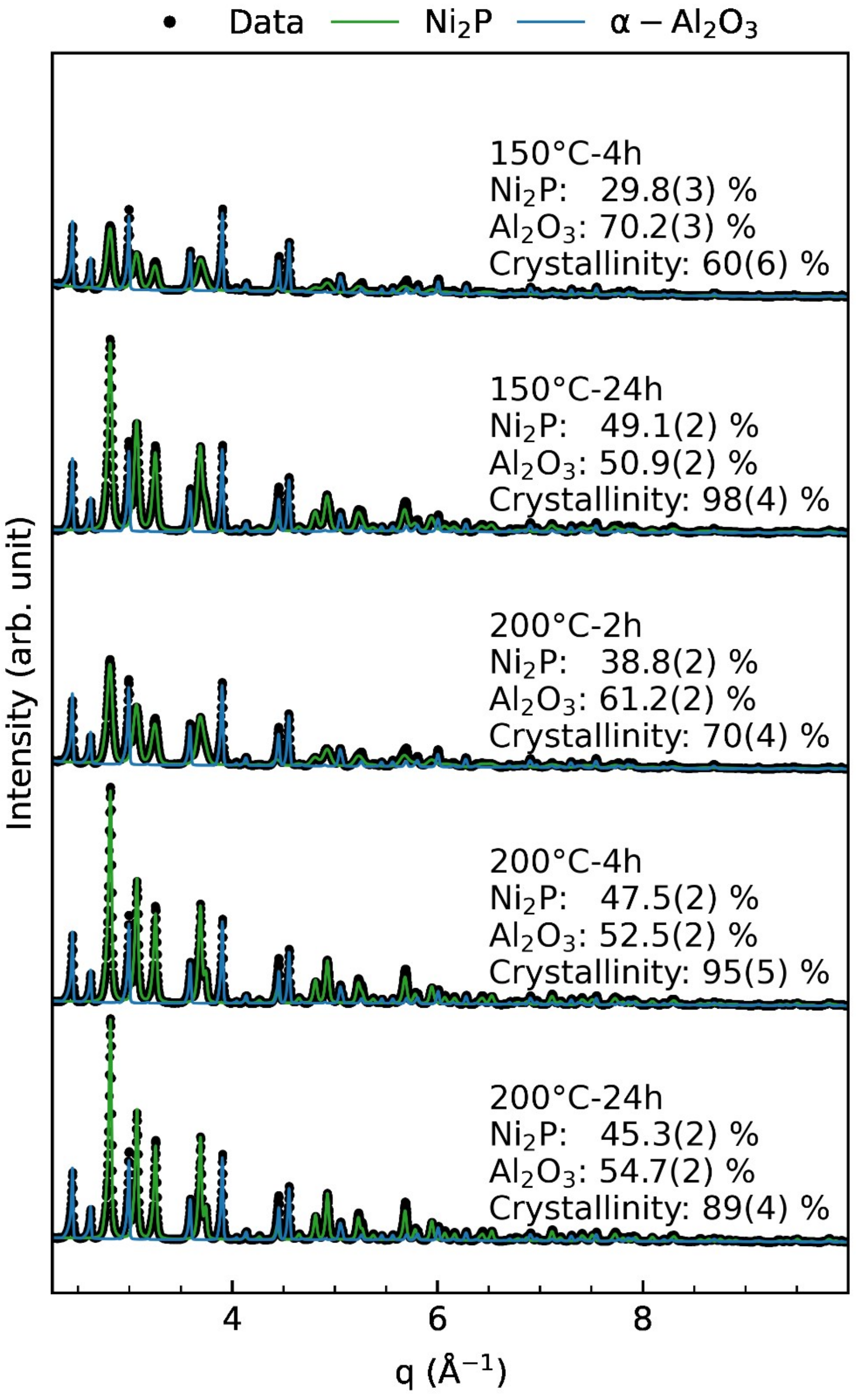

Figure S 21. Diffractograms of the synthesis products mixed with Al_2O_3. For each case, the crystallinity is determined.

S6: Additional STEM images

Figure S22, S26, S28, S30 and S32 shows additional stem images of the Ni_2P samples: 150°C-4h, 150°C-24h, 200°C-2h, 200°C-4h, and 200°C-24h. These particles have an approximate size of 20 nm, 20 nm, 25 nm, 25 nm, and 30 nm according to PXRD.

Figure S23 shows a STEM-EDS image for ~20 nm Ni_2P sample 150°C-4h with the corresponding spectrum shown in Figure S24.

Figures S25, S27, S29, S31, and S33 show the spectrum from the STEM-EDS images in the main article.

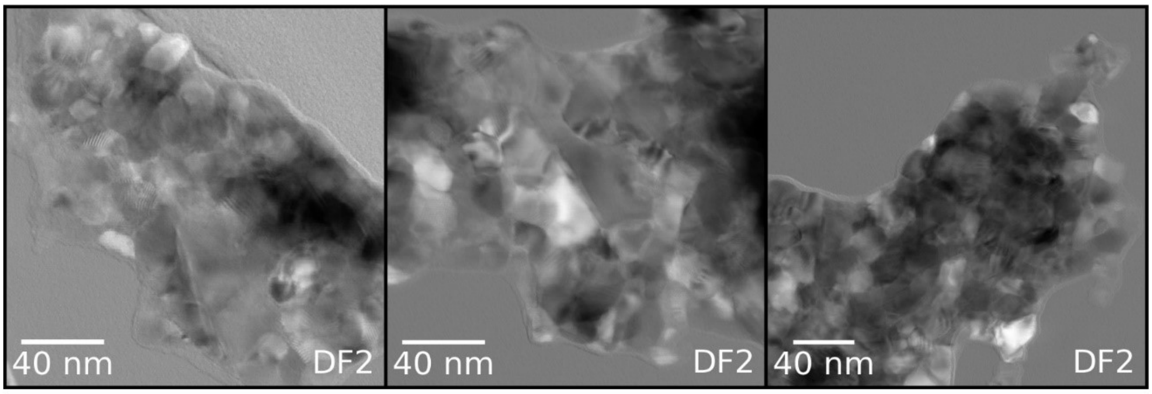

Figure S22. STEM images of Ni_2P 150°C-4h.

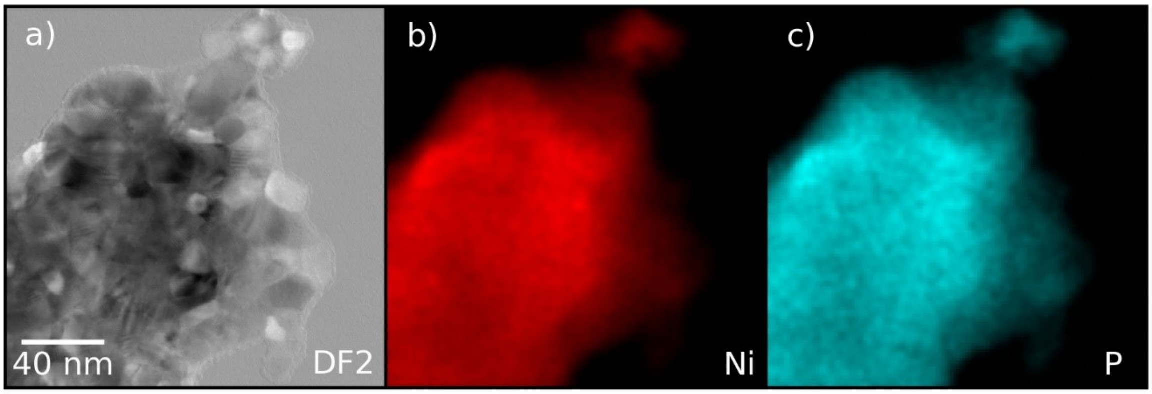

Figure S23. STEM-EDS images of Ni_2P 150°C-4h.

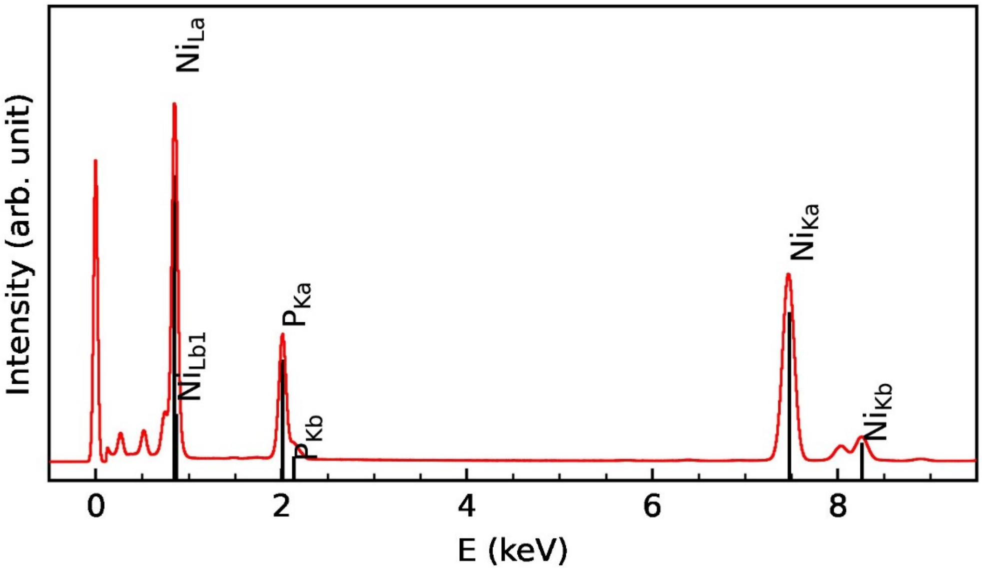

Figure S24. Spectrum from the STEM-EDS image shown in Figure S22.

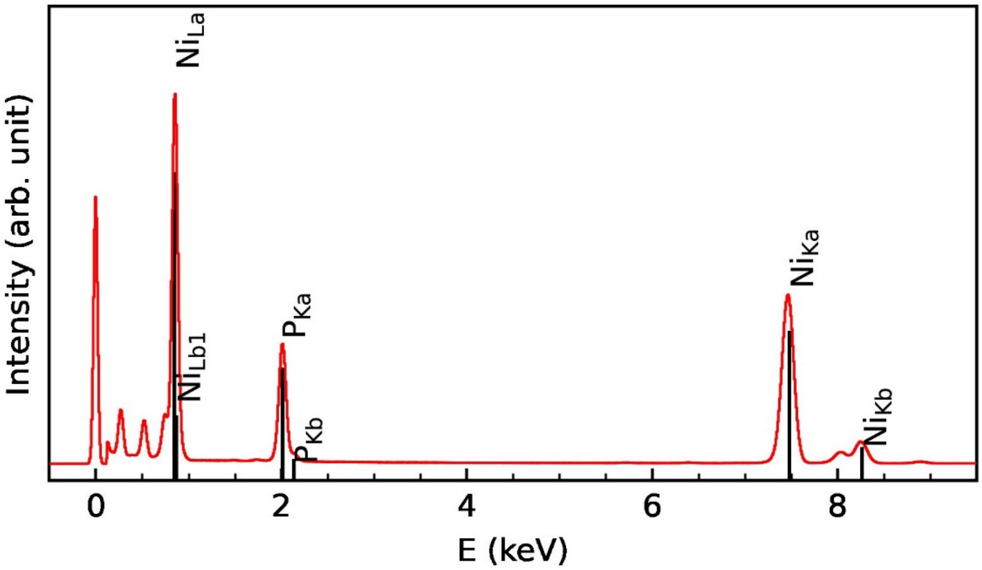

Figure S25. Spectrum from the STEM-EDS image shown in Figure 6a), b), and c).

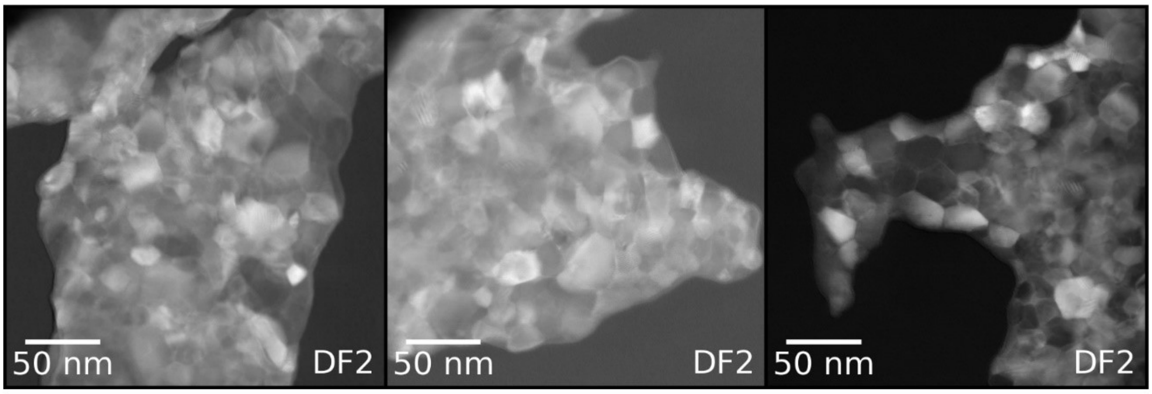

Figure S26. STEM images of Ni_2P 150°C-24h**.**

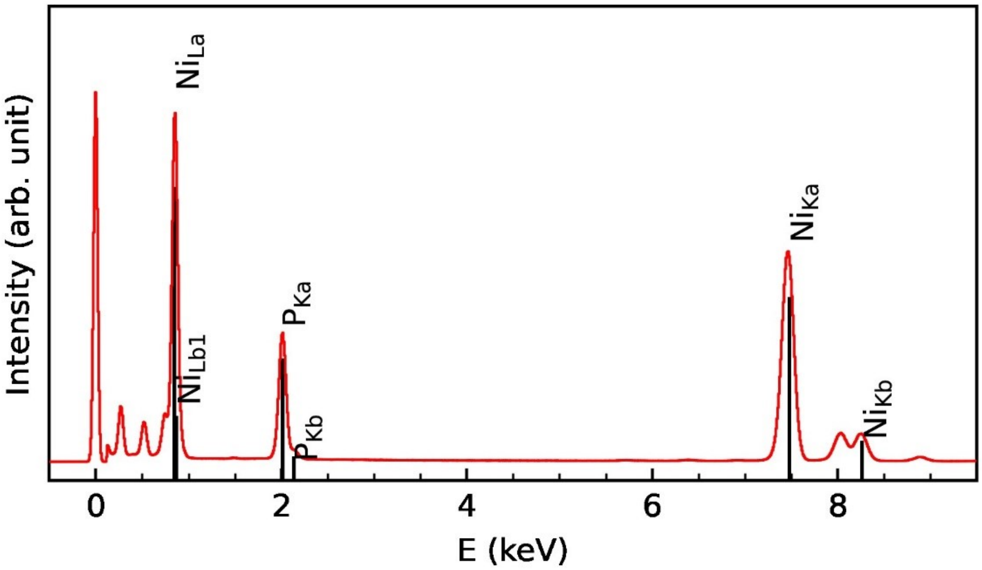

Figure S27. Spectrum from the STEM-EDS image shown in Figure 6d), e), and f).

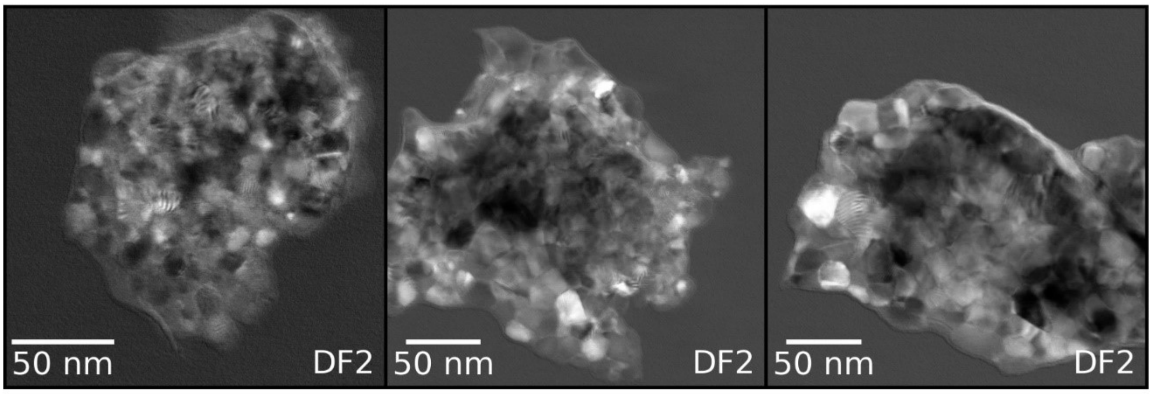

Figure S28. STEM images of Ni_2P 200°C-2h**.**

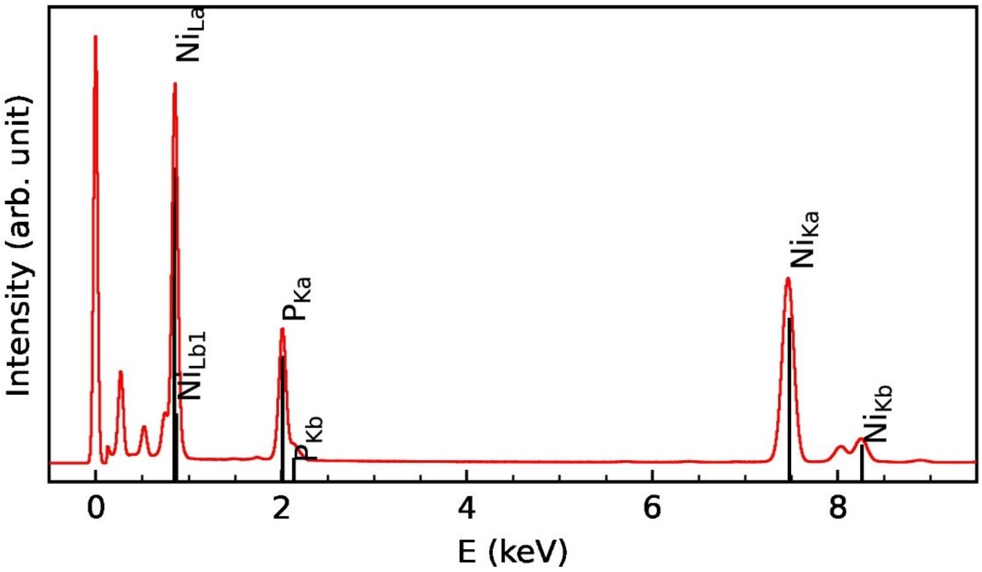

Figure S29. Spectrum from the STEM-EDS image shown in Figure 6g), h), and i).

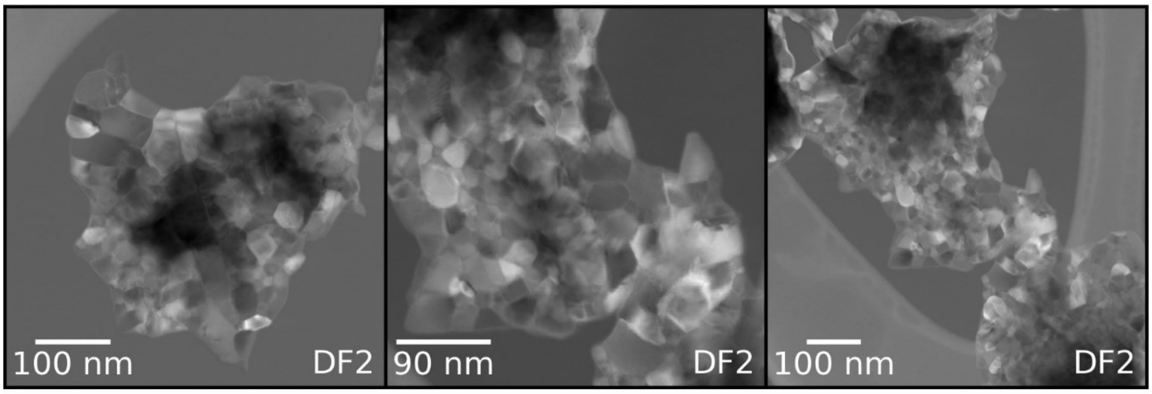

Figure S30. STEM images of Ni_2P 200°C-4h.

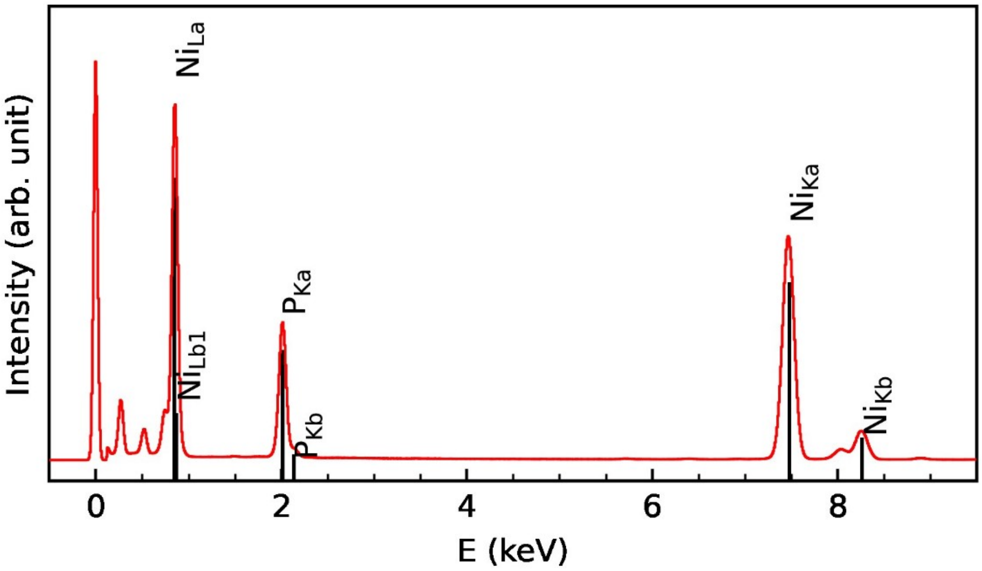

Figure S31. Spectrum from the STEM-EDS image shown in Figure 6j), k), and l).

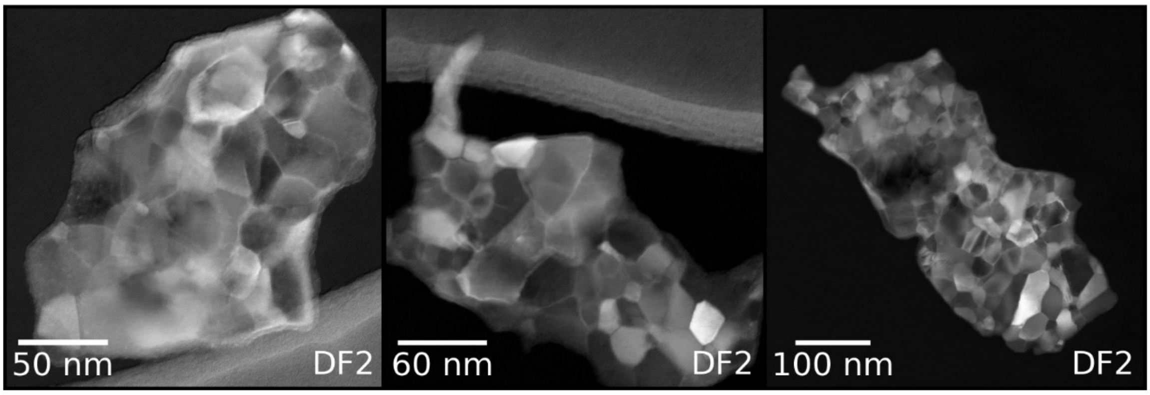

Figure S32. STEM images of Ni_2P 200°C-24h.

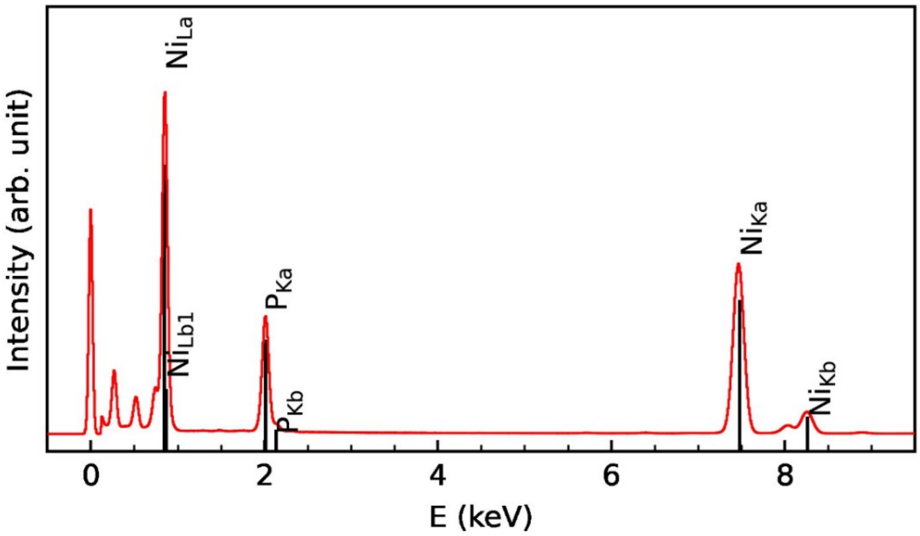

Figure S33. Spectrum from the STEM-EDS image shown in Figure 6m), n), and o).

S7: Whole powder pattern modeling.

For the three most crystalline Ni_2P *ex situ* samples with a size of ~20 nm, ~25 nm, and ~30 nm, whole powder pattern modeling (WPPM) is performed to obtain the size distribution. This section visually shows the fits in Figures S34, S35, and S36 obtained by WPPM. Furthermore, Table S6 compares the refined unit cell size and average particle size with the values obtained by Rietveld refinement.

Table S6. Results from WPPM compared to the results obtained from normal Rietveld refinement.

		Rietveld				WPPM				
T (°C)	t (h)	a (Å)	c (Å)	Size (nm)	R_{wp}	a (Å)	c (Å)	Size (nm)	std	R_{wp}
150	24	5.8696(1)	3.3902(1)	19.50(8)	3.55	5.8695(1)	3.39008(8)	23.0(14)	8.3(9)	3.01
200	4	5.86725(8)	3.39006(6)	25.78(9)	3.71	5.86722(6)	3.39005(4)	33.3(10)	10.0(7)	2.81
200	24	5.86652(6)	3.38980(4)	29.52(8)	3.69	5.86649(4)	3.38979(3)	37.2(8)	11.4(5)	2.74

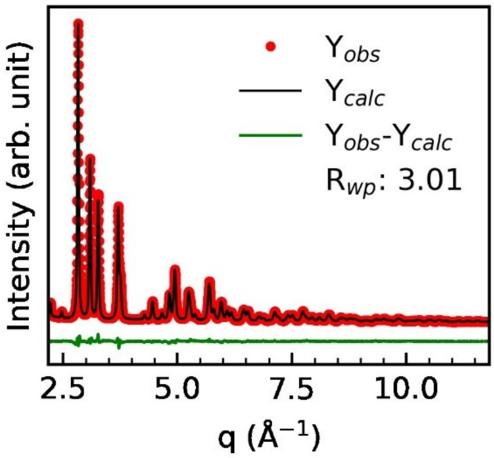

Figure S34. WPPM, 150 °C and 24 h.

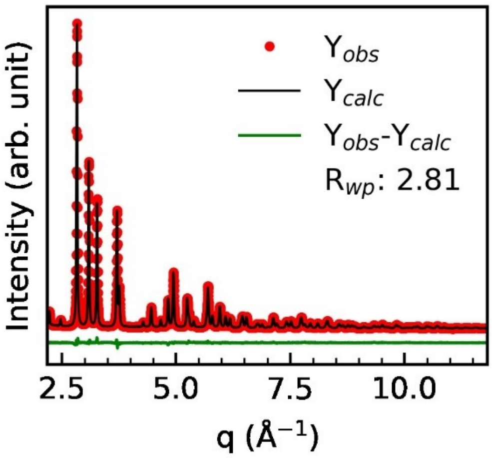

Figure S35. WPPM, 200 °C and 4 h.

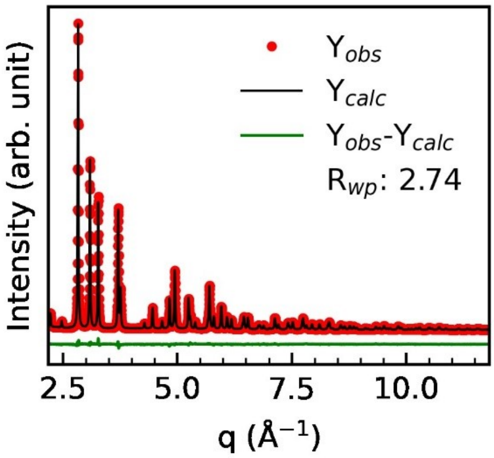

Figure S36. WPPM, 200 °C and 24 h.

S8: Electrochemical measurements

Between measurements, the RDE was polished with water-based suspension of 9, 3, 1, and 0.25 µm diamond (Struers ApS) on a polishing microcloth. The electrodes were sonicated several times in deionized water and absolute ethanol for 30 min to remove the excess suspension. The polished electrode was pretreated by 20 cyclic voltammetry (CV) scans from -0,4 to 1 V versus $E_{Hg/HgO}$, then rinsed using absolute ethanol before loading the catalyst ink.

An oxidized or contaminated glassy carbon induces a high charge transfer resistance between RDE and a catalyst layer. This phenomenon can be described as a complex element (QR), in which the constant phase element (Q) and resistor (R) are connected in parallel. The complex element (QR) exhibits a peak in the frequency-dependent phase angle of the impedance in the non-Faradic region.[3] We confirm the appropriate condition of the working electrode after the activating process by Potentiostatic electrochemical impedance spectroscopy (EIS) measurements at 0.0 V versus Hg/HgO in the non-Faradic region. The Bode plots of EIS show no peak, indicating no parasitic Q in the working electrode.

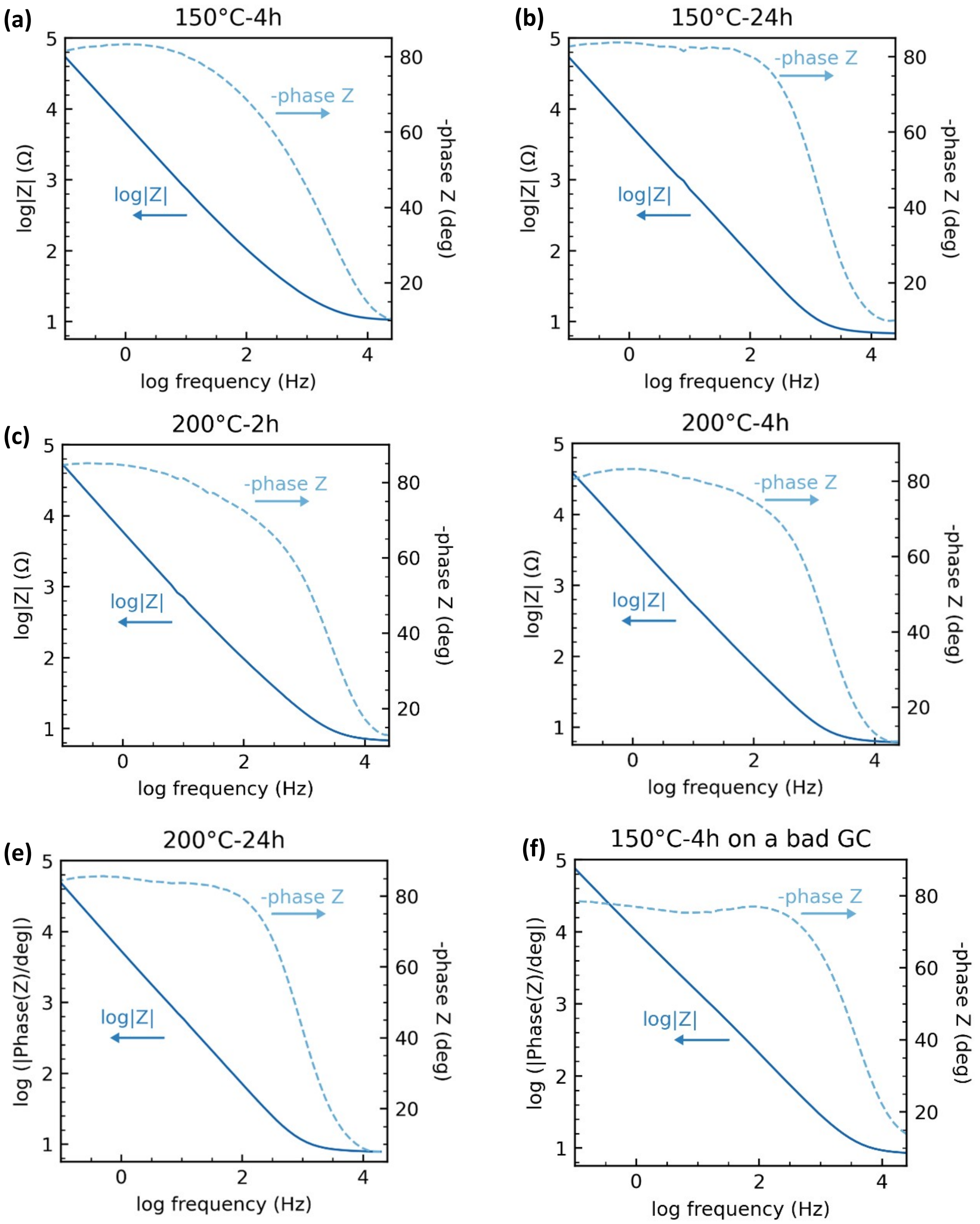

Figure S37. Bode plots for electrochemical impedance spectroscopy data obtained at 0.0 V versus Hg/HgO of (a) 150°C-4h, (b) 150°C-24h, (c) 200°C-2h, (d) 200°C-4h, (e) 200°C-24h, and (f) 150°C-24h on a bad glassy-carbon electrode (GC).

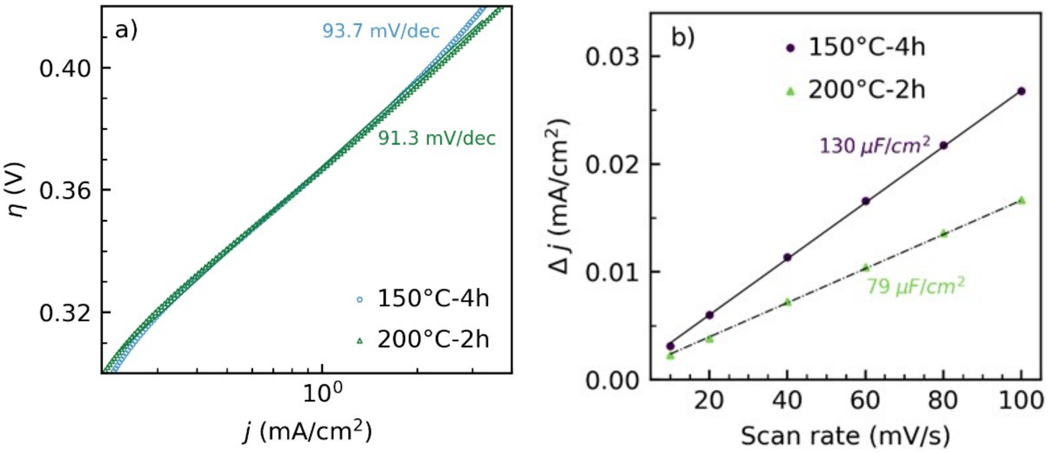

Figure S38. Electrocatalytic activity of the electrodes for OER in 1 M KOH solution using 150°C-4h and 200°C-2h samples. a) Tafel plots, b) Charging current density differences Δj at 0.1 V vs. Hg/HgO plotted against scan rates. The linear slope is twice that of the double-layer capacitance (Cdl).

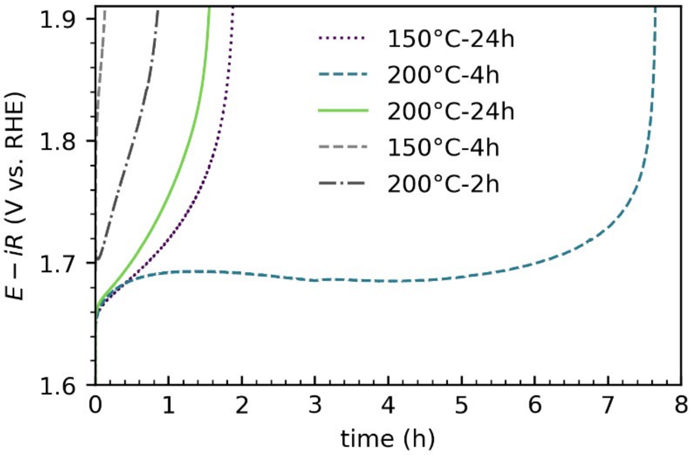

Figure S39. Potentials required for 10 mA cm^{-2} current density from the chronopotentiometry measurements for OER in 1 M KOH solution.

The frequency-dependent phase angle of the obtained EIS spectra exhibited three overlapping components, indicating the coexistence of three constant phase processes. The high-frequency component, above 1000 Hz, corresponds to the charge-discharge of the electric double layer at the electrode and electrolyte interface. The other lower frequency components can be assigned to inactive and active sites due to incomplete coverage of the catalyst layer on the GC electrode and the possible presence of an oxidized surface layer.[4]

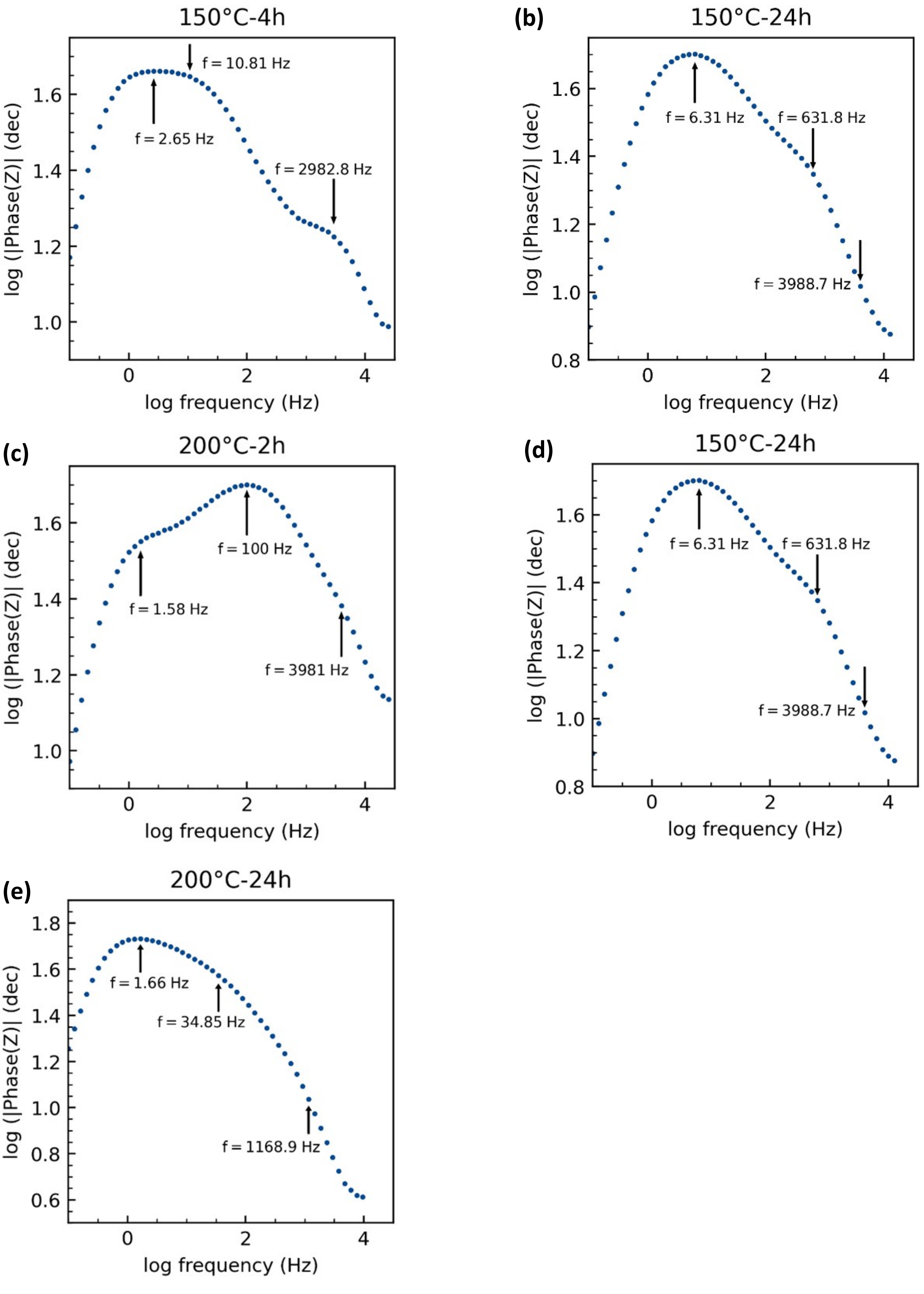

Figure S40. Bode plot for electrochemical impedance spectroscopy data obtained at 0.65 V versus Hg/HgO of (a) 150°C-4h, (b) 150°C-24h, (c) 200°C-2h, (d) 200°C-4h, (e) 200°C-24h samples.

The EIS spectra could be fitted using a model shown in Figure S41a. In this model, three complex elements, consisting of Q_i and R_i are connected in parallel, (Q_1R_1), (Q_2R_2), and (Q_3, R_3) represent the interfaces of working electrode-electrolyte, inactive site-electrolyte, and active site-electrolyte, respectively. R_0 represents the uncompensated solution resistance, which is employed for performing iR-corrections of the data. The fitted values are listed in Table S7.

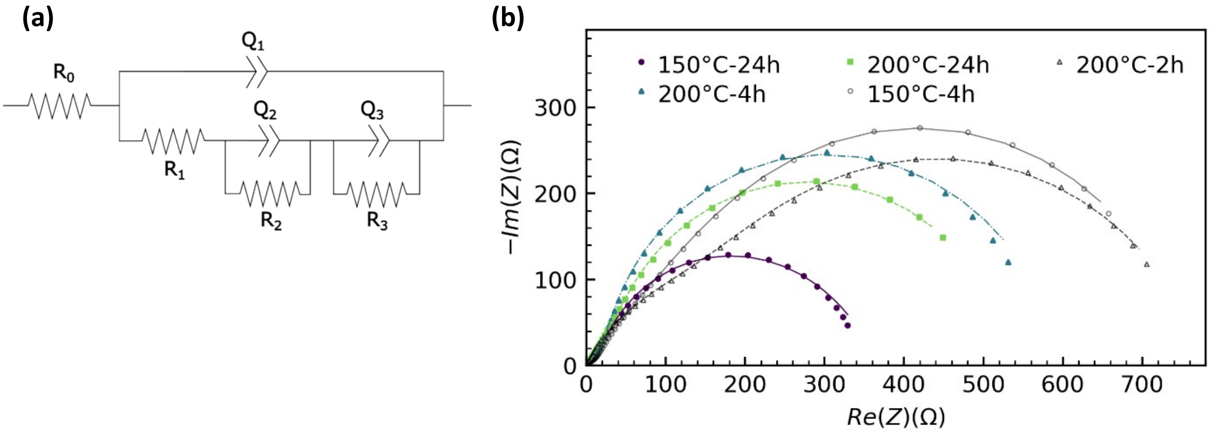

Figure S41. a) Equivalent circuit model employed for fitting EIS data. b) Nyquist plots for EIS measured at the potential of 0.62 V (vs Hg/HgO).

Table S7. Parameters obtained from the fitting using the equivalent circuit modeling.

Sample	R_0 (Ω)	R_1 (Ω)	Q_1 mF.s$^{\alpha-1}$	α_1	R_2 (Ω)	Q_2 mF.s$^{\alpha-1}$	α_2	R_3 (Ω)	Q_3 mF.s$^{\alpha-1}$	α_3
150°C-4h	9.53	15.3	0.704	0.70	158.1	0.730	0.68	591.7	0.807	0.90
150°C-24h	6.32	23.2	0.613	0.68	35.8	0.486	0.85	308.5	0.300	0.97
200°C-2h	5.67	19.8	0.175	0.71	234.6	0.078	0.71	528.9	0.519	0.83
200°C-4h	5.77	17.6	0.414	0.74	29.9	0.910	0.78	558.5	0.421	0.99
200°C-24h	7.52	12.3	0.520	0.77	39.8	1.217	0.70	502.3	0.822	0.90

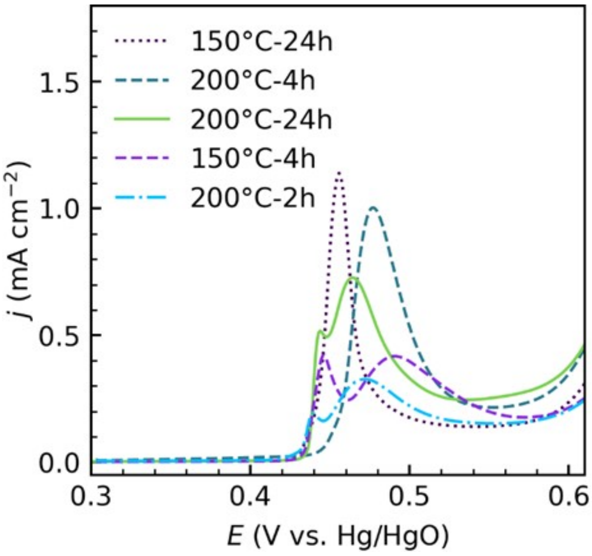

Figure S42. iR-corrected polarization curves of Ni_2P nanoparticles on GC in the region of the oxidation of Ni(II) to Ni(III). The measurements were carried out at a scan rate of 5 mV/s.

Figure S42 shows the iR-corrected CVs between 0.43 and 0.57 V vs. Hg/HgO corresponding to the $Ni(OH)_2$/NiOOH transition. As is apparent from the figure, the 150°C-4h and 200°C-2h samples, containing amorphous phosphorus, exhibit a lower oxidation of $Ni(OH)_2$ to NiOOH, which agrees with their lower catalytic activities compared with the fully crystalline Ni2P samples. The 150°C-4h, 200°C-2h, and 200°C-24h samples show two peaks in the oxidation region, indicating that their outer layers possibly include two conversions: α-$Ni(OH)_2$ to γ-NiOOH and β-$Ni(OH)_2$ to β-NiOOH.[5, 6] On the other hand, the 150°C-24h samples exhibit a single peak at 0.45V vs. Hg/HgO, corresponding to a conversion of α-$Ni(OH)_2$ to γ-NiOOH, while the 200°C-4h sample shows a peak at 0.47 V vs. Hg/HgO, corresponding to a conversion of β-$Ni(OH)_2$ to β-NiOOH.

S9: SEM-EDS images of electrodes before and after OER.

The Ni_2P thin films from before and after electrochemical measurements are characterized by SEM-EDS and PXRD. Figure S42-S51 shows SEM-EDS images of the five Ni_2P thin films used for electrochemistry before and after performing the measurements. Figure S52-S56 shows the corresponding diffractograms.

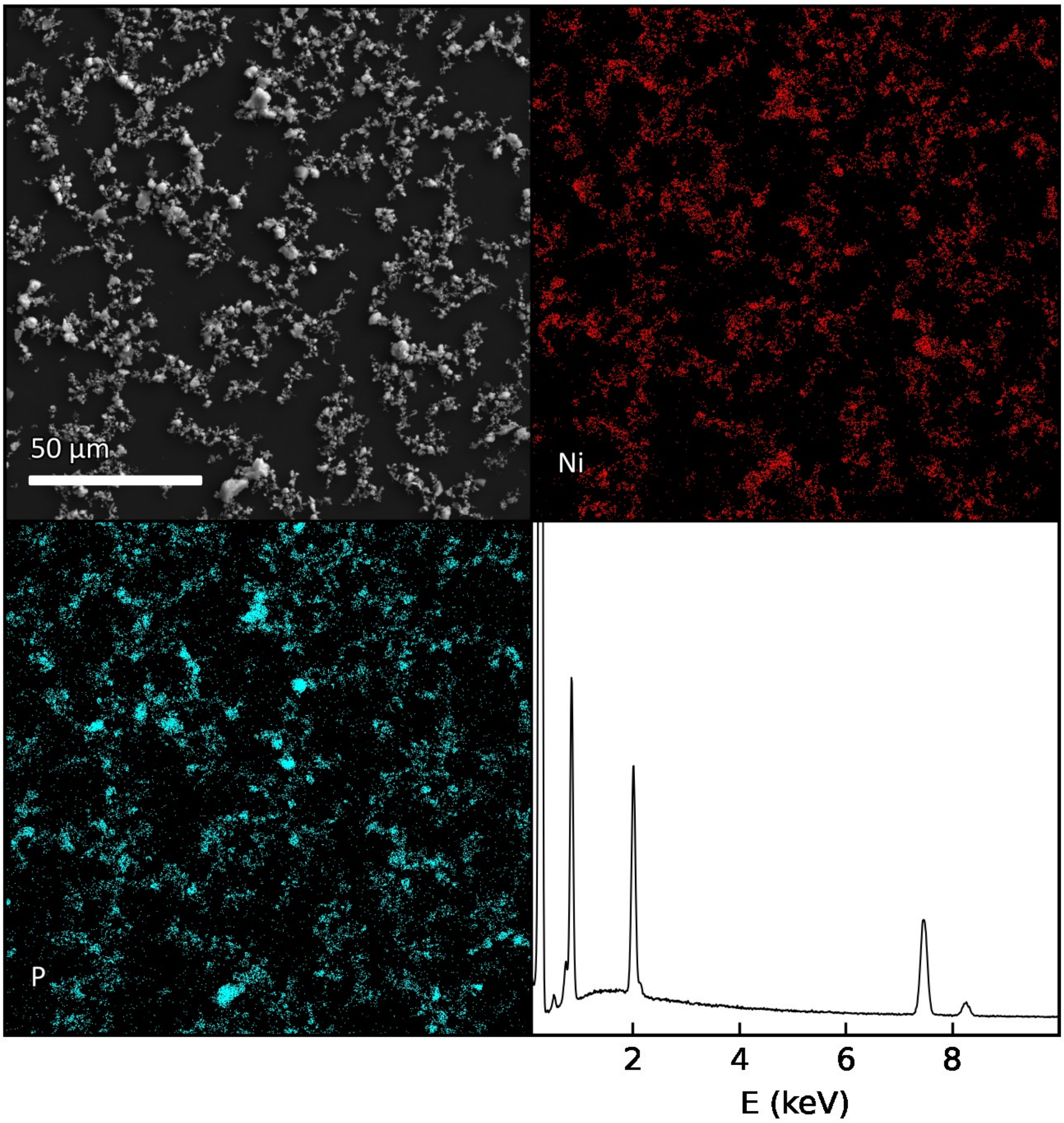

Figure S43. SEM-EDS image of a Ni_2P thin film before electrochemical measurement. The thin film is produced using Ni_2P from the ex situ synthesis at 150 °C for 4 h.

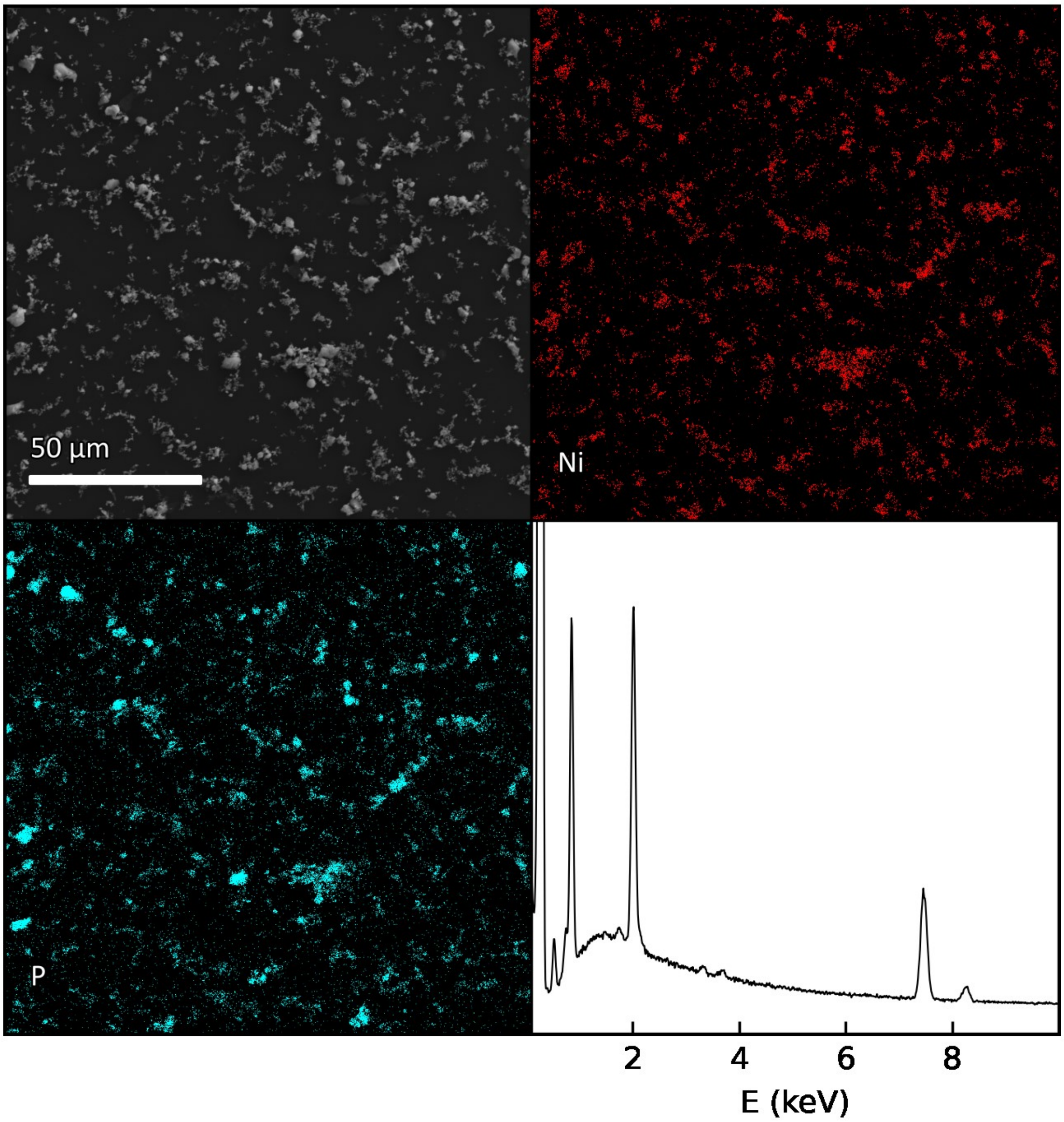

Figure S44. SEM-EDS image of a Ni_2P thin film after electrochemical measurement. The thin film is produced using Ni_2P from the ex situ synthesis at 150 °C for 4 h.

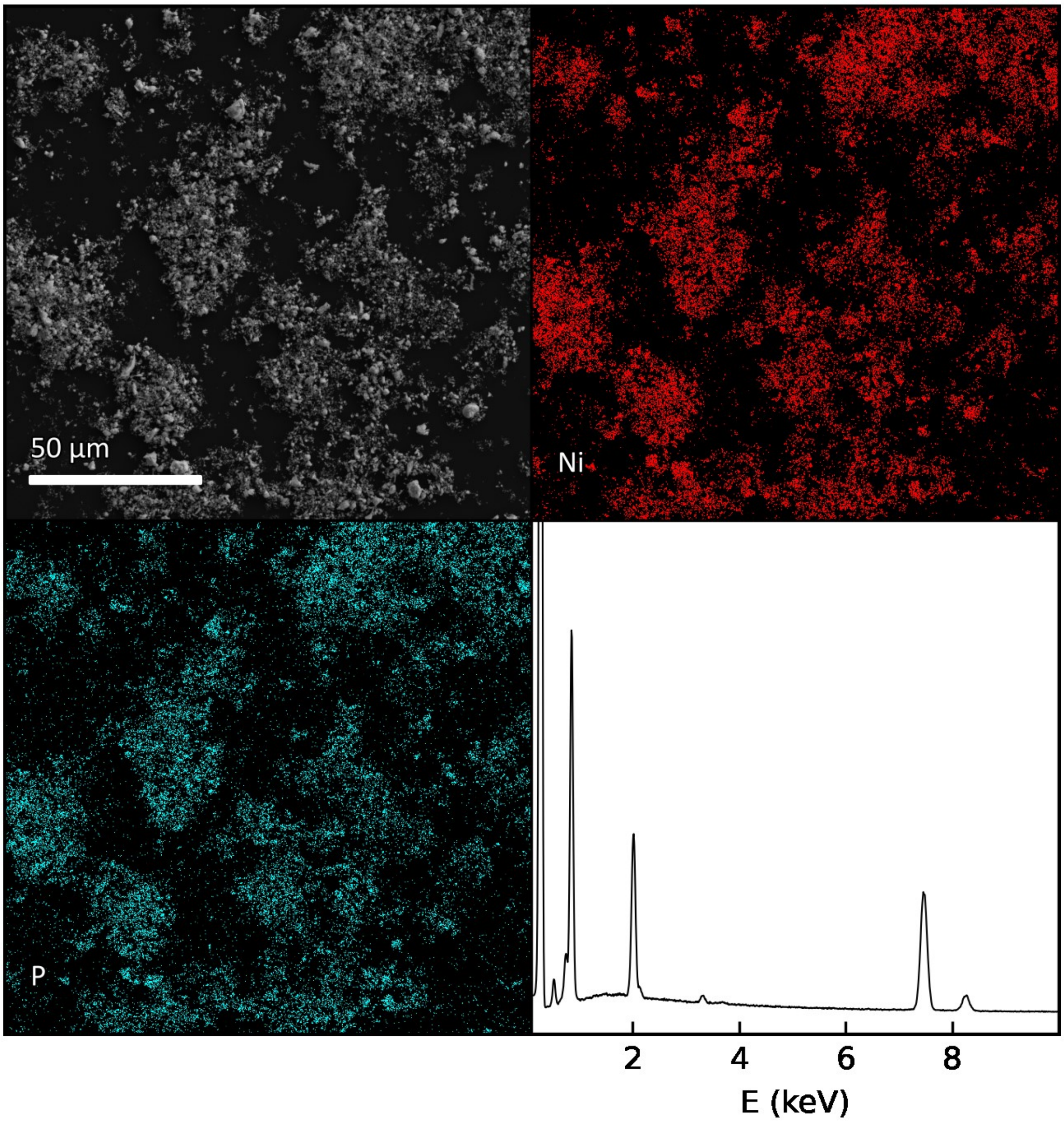

Figure S45. SEM-EDS image of a Ni_2P thin film before electrochemical measurement. The thin film is produced using Ni_2P from the ex situ synthesis at 150 °C for 24 h.

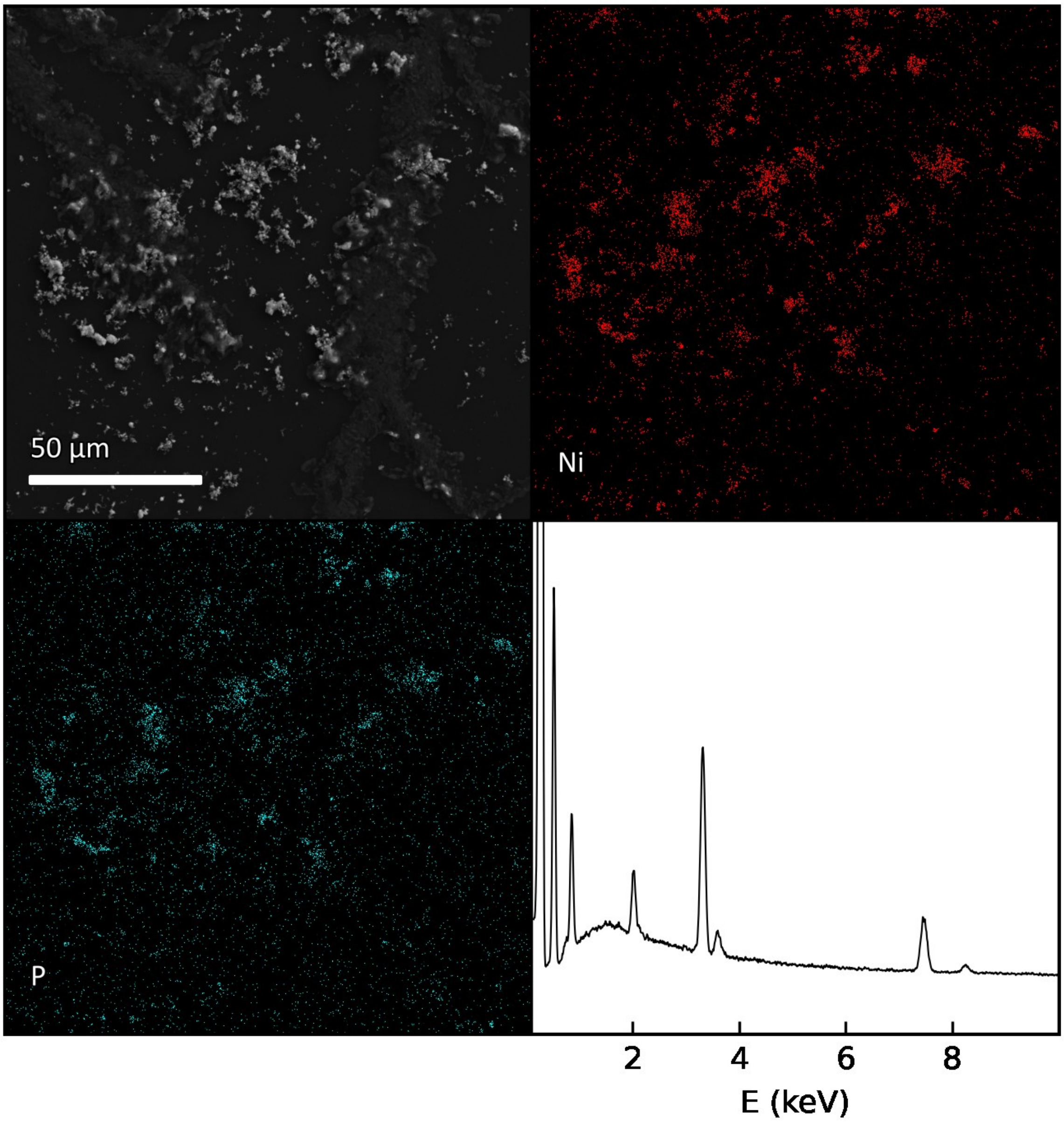

Figure S46. SEM-EDS image of a Ni_2P thin film after electrochemical measurement. The thin film is produced using Ni_2P from the ex situ synthesis at 150 °C for 24 h.

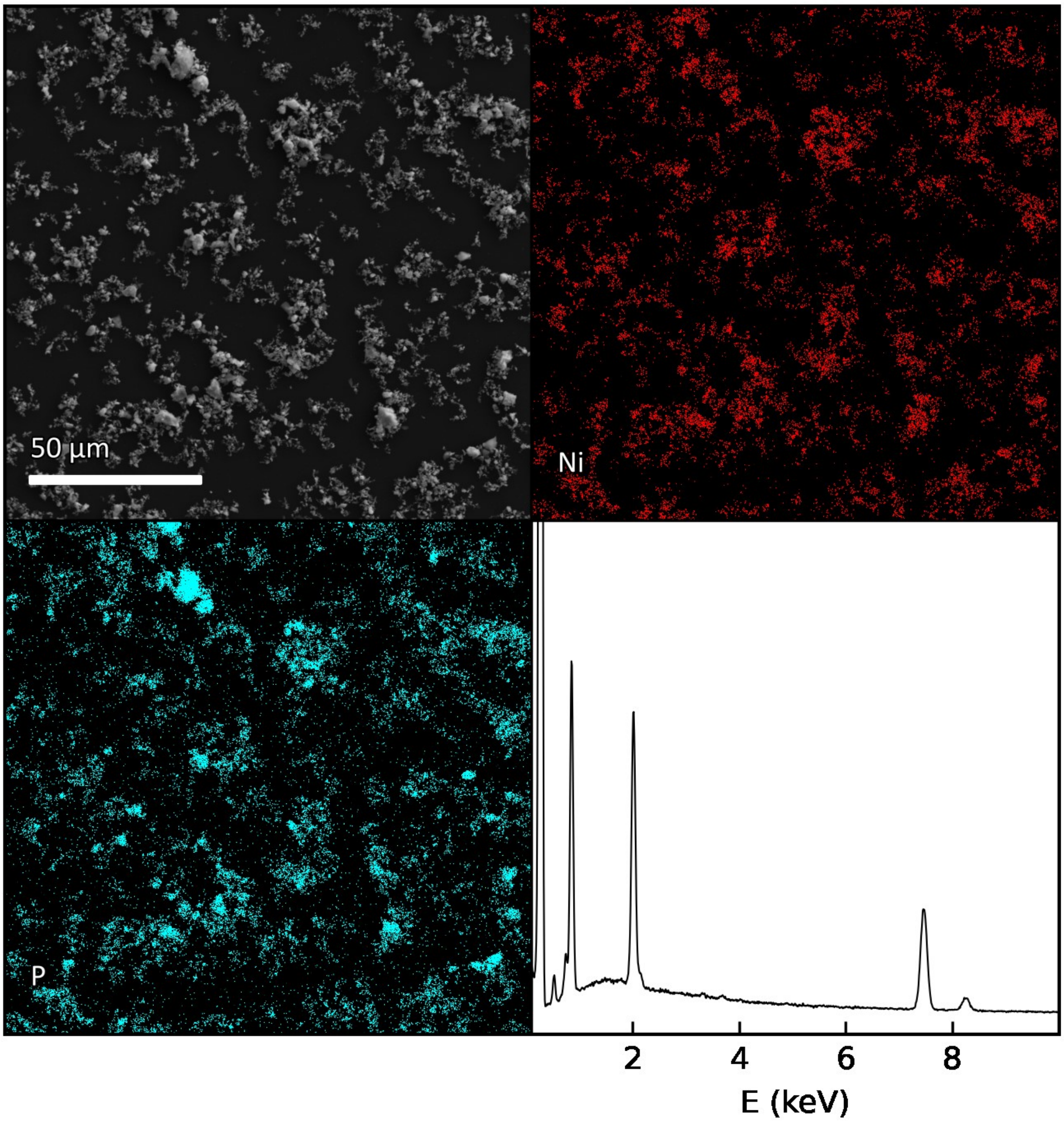

Figure S47. SEM-EDS image of a Ni_2P thin film before electrochemical measurement. The thin film is produced using Ni_2P from the ex situ synthesis at 200 °C for 2 h.

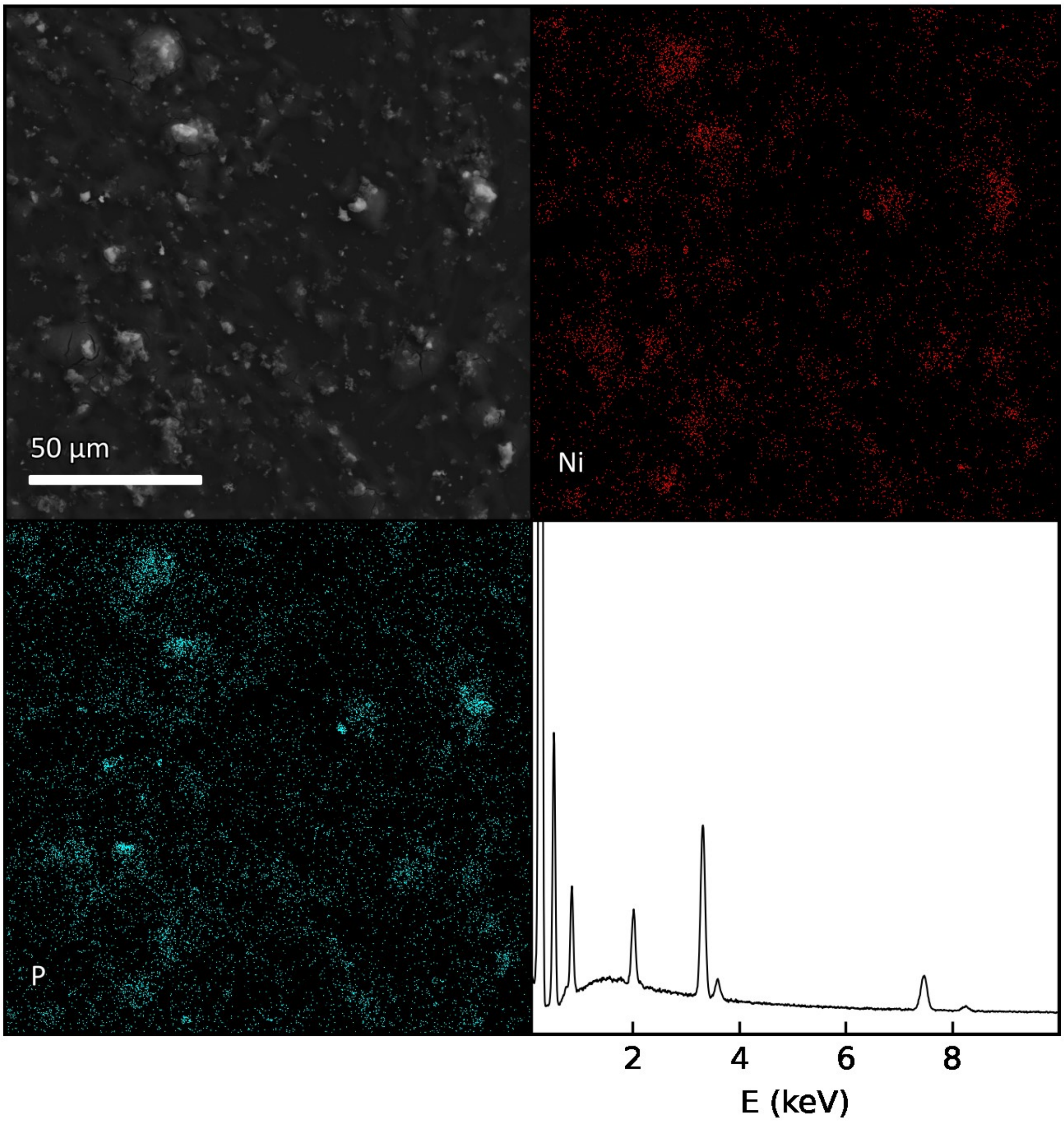

Figure S48. SEM-EDS image of a Ni_2P thin film after electrochemical measurement. The thin film is produced using Ni_2P from the ex situ synthesis at 200 °C for 2 h*.*

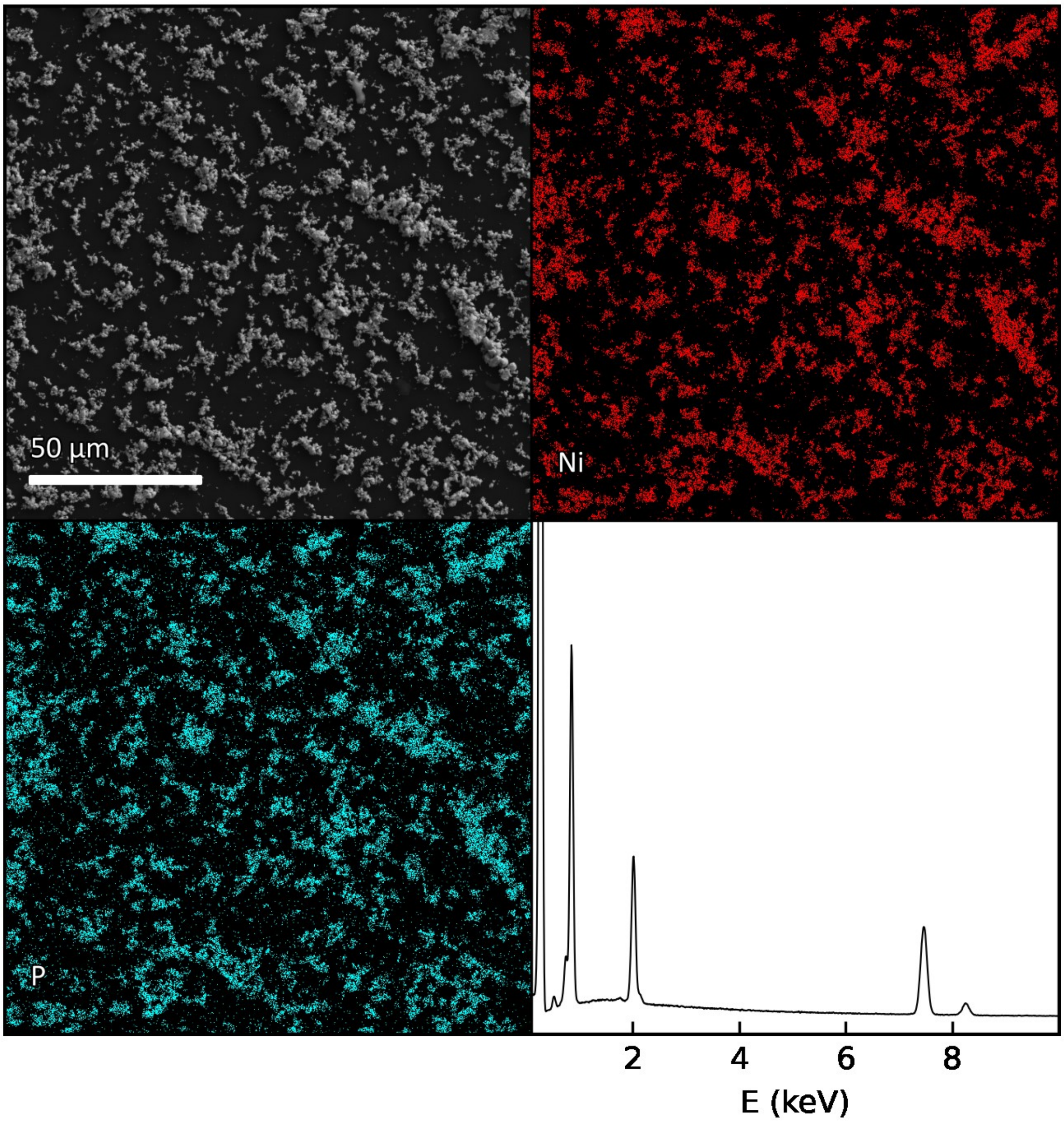

Figure S49. SEM-EDS image of a Ni_2P thin film before electrochemical measurement. The thin film is produced using Ni_2P from the ex situ synthesis at 200 °C for 4 h.

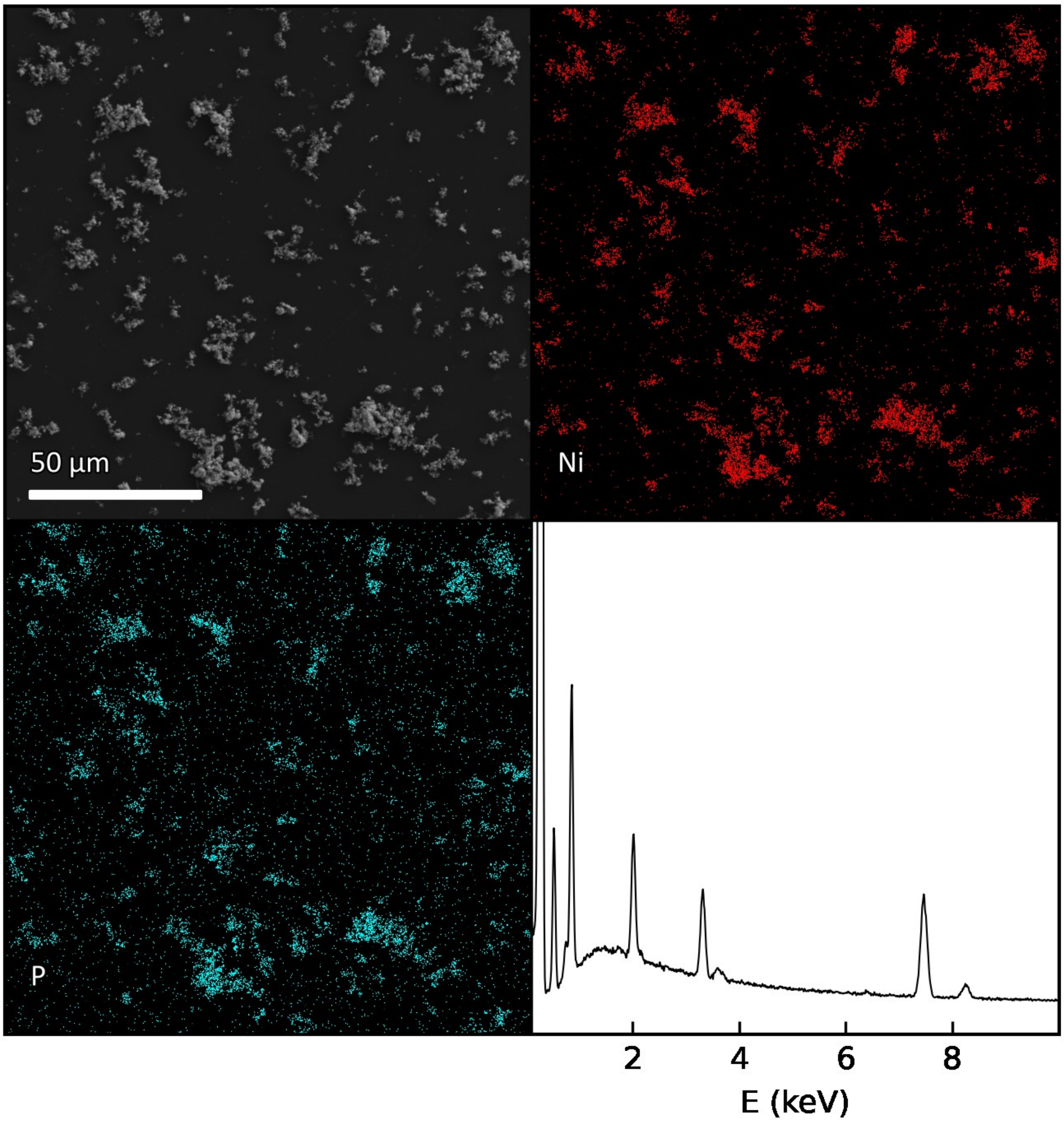

Figure S50. SEM-EDS image of a Ni_2P thin film after electrochemical measurement. The thin film is produced using Ni_2P from the ex situ synthesis at 200 °C for 4 h.

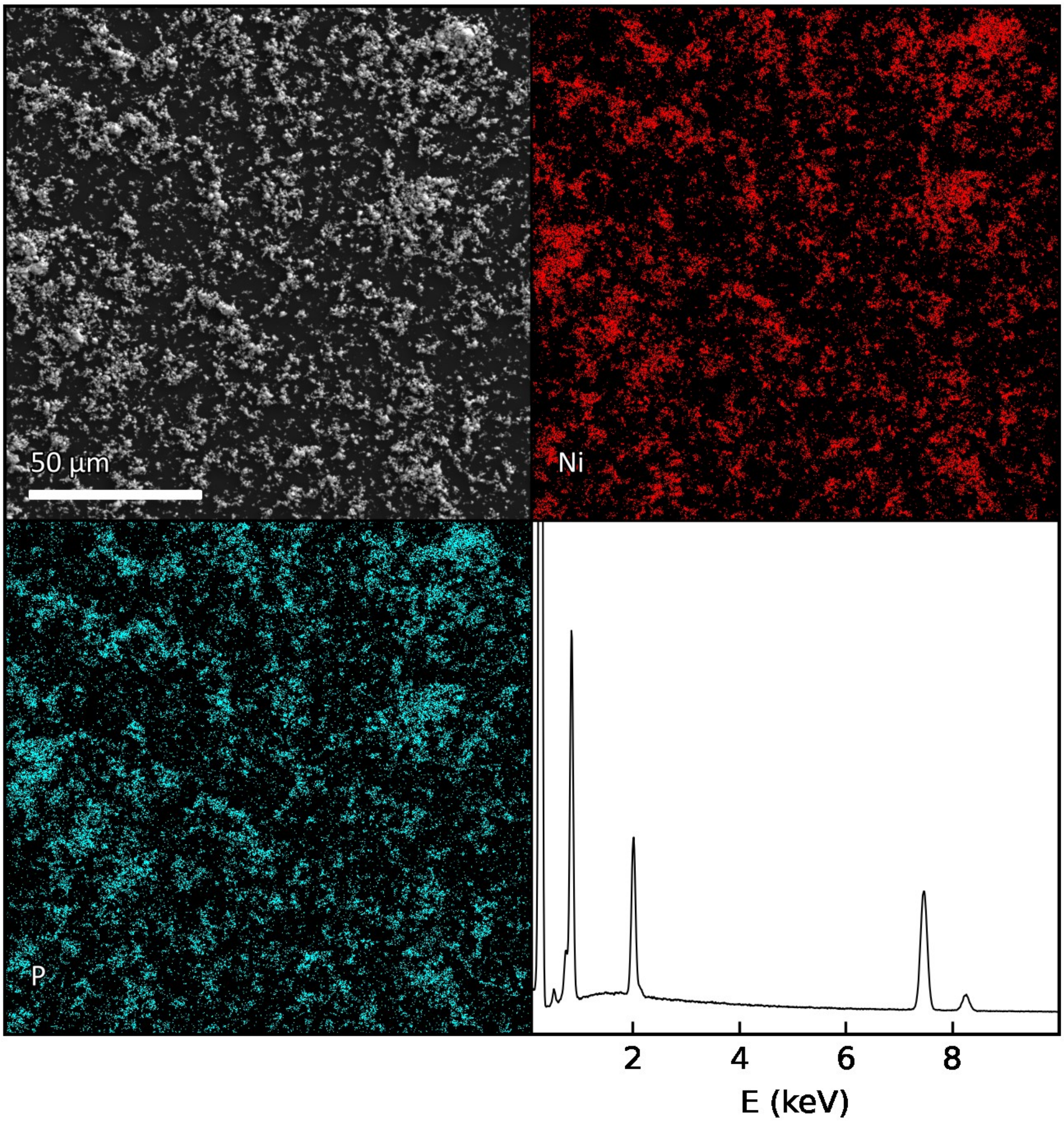

Figure S51. SEM-EDS image of a Ni_2P thin film before electrochemical measurement. The thin film is produced using Ni_2P from the ex situ synthesis at 200 °C for 24 h.

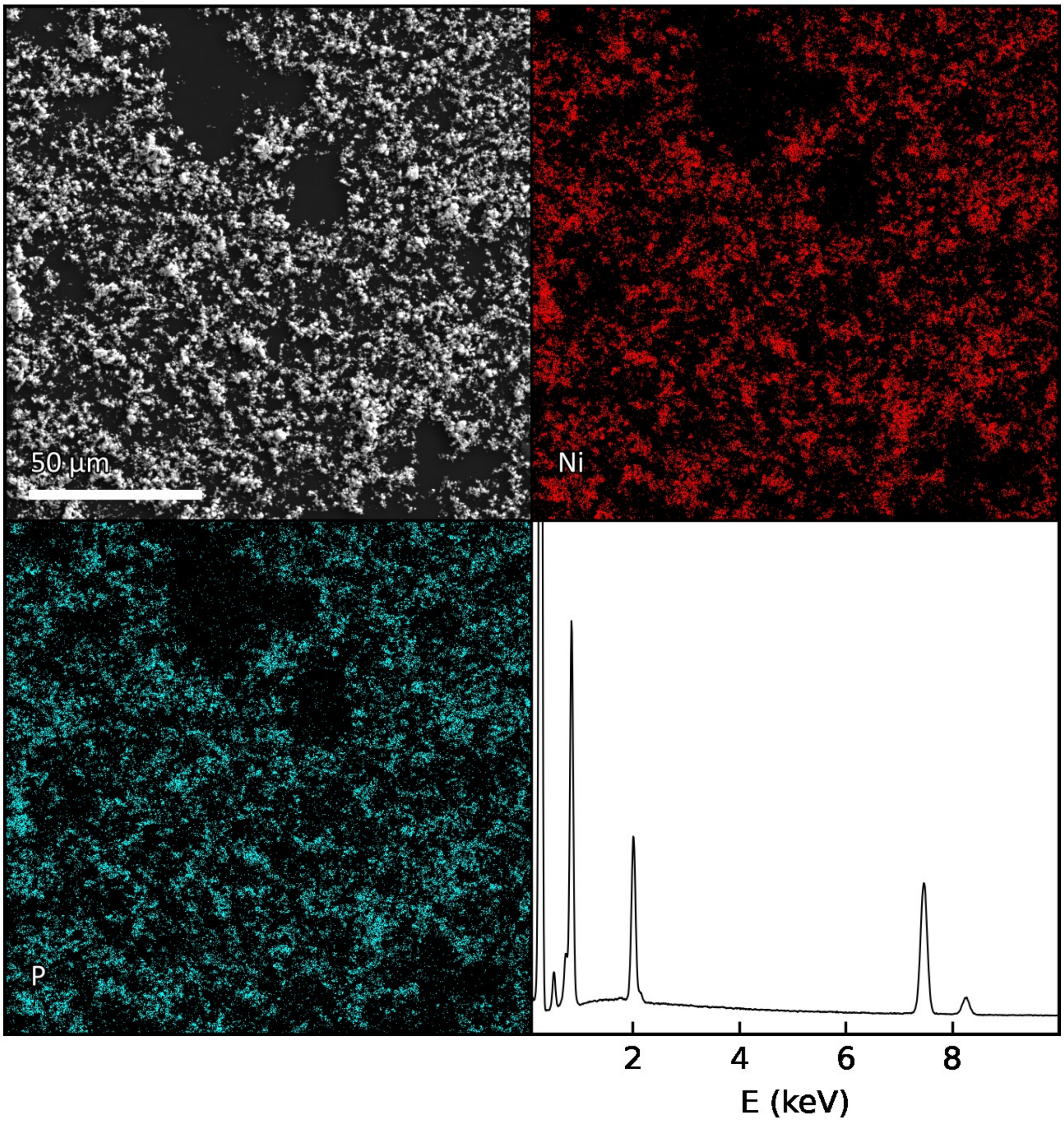

Figure S52. SEM-EDS image of a Ni_2P thin film after electrochemical measurement. The thin film is produced using Ni_2P from the ex situ synthesis at 200 °C for 24 h.

References

1. L. M. Yupko, A. A. Svirid and S. V. Muchnik, *Powder Metall. Met. Ceram.*, 1986, **25**, 768-773.
2. S. N. Britvin, M. N. Murashko, M. G. Krzhizhanovskaya, O. S. Vereshchagin, Y. Vapnik, V. V. Shilovskikh, M. S. Lozhkin and E. V. Obolonskaya, *Am. Mineral.*, 2022, **107**, 1946-1951.
3. A. C. Lazanas and M. I. Prodromidis, *ACS Meas. Sci. Au*, 2023, **3**, 162-193.
4. R. L. Doyle and M. E. G. Lyons, *Journal of The Electrochemical Society*, 2013, **160**, H142.
5. R. Barnard, C. F. Randell and F. L. Tye, *J. Appl. Electrochem.*, 1980, **10**, 109-125.
6. S. Klaus, Y. Cai, M. W. Louie, L. Trotochaud and A. T. Bell, *J. Phys. Chem. C*, 2015, **119**, 7243-7254.